J. Fluid Mech. (2010), *vol.* 642, *pp.* 15–48.
doi:10.1017/S0022112009991686

Strong non-Boussinesq effects near the onset of convection in a fluid near its critical point

GUENTER AHLERS[1]†, BERND DRESSEL[2], JAECHUL OH[3] AND WERNER PESCH[2]

[1]Department of Physics, University of California, Santa Barbara, CA 93106, USA

[2]Physikalisches Institut, Universität Bayreuth, D-95440 Bayreuth, Germany

[3]Plasma Physics Division, U.S. Naval Research Laboratory, Washington, DC 20375, USA

(Received 23 March 2009; revised 13 August 2009; accepted 14 August 2009; first published online 16 November 2009)

Measurements of fluctuations and convection patterns in horizontal layers of fluid heated from below and near the onset of Rayleigh–Bénard convection (RBC) are reported under conditions where the fluid properties vary strongly over the temperature range $\Delta T = T_b - T_t$ (T_b and T_t are the temperatures at the bottom and top of the sample, respectively). To facilitate a comparison with the data, the theory of Busse (*J. Fluid Mech.*, vol. **30**, 1967, p. 625) of these so called non-Oberbeck–Boussinesq (NOB) effects, which applies to the case of relatively weak (and linear) temperature dependences, was extended to arbitrary variations with temperature. It is conceptually useful to divide the variations with temperature of the fluid properties into two disjunct parts. One part is chosen so that it preserves the reflection symmetry of the system about the horizontal midplane, while the remainder breaks that symmetry. The latter, exclusively considered by Busse, leads (in contrast to the formation of the typical convection *rolls* in RBC) to *hexagons* immediately above the transition to convection at the critical temperature difference ΔT_c. The symmetric part, on the other hand, does not prevent the bifurcation to rolls, but may become very important for the determination of ΔT_c. In the experiment the fluid was sulfur hexafluoride at temperatures above but close to the gas–liquid critical point, where all fluid properties vary strongly with temperature. All measurements were done along isobars by varying ΔT. Patterns were observed above onset ($\Delta T \gtrsim \Delta T_c$), while for the conduction state at $\Delta T < \Delta T_c$ there were only fluctuations induced by Brownian motion. When the mean temperature $T_m = (T_b + T_t)/2$ was such that the density ρ at T_m was equal to the critical density ρ^*, the mirror symmetry about the horizontal midplane of the sample was essentially preserved. In that case, as expected, we found a direct transition to rolls and the critical temperature difference ΔT_c was considerably shifted compared to the critical value $\Delta T_{c,OB}$ in the absence of NOB effects. When, on the other hand, T_m was not located on the critical isochore, the NOB effects broke the reflection symmetry and led to a hysteretic transition from fluctuations to hexagonal patterns. In this latter case the hexagonal pattern, the observed hysteresis at onset and the transition from hexagons to rolls at larger ΔT were consistent with the 'classical' predictions by Busse.

Key words: Bénard, instability

† Email address for correspondence: guenter@physics.ucsb.edu

1. Introduction

Convection of a fluid confined between two parallel horizontal plates and heated from below (Rayleigh–Bénard convection or RBC) is a standard paradigm of pattern-forming instabilities in spatially extended nonlinear systems (see for instance Bodenschatz, Pesch & Ahlers 2000). The main control parameter is the temperature difference ΔT across the fluid layer between the bottom plate (at temperature $T = T_b$) and the top plate (at $T = T_t < T_b$). The critical temperature difference ΔT_c is defined as the smallest ΔT at which the spatially uniform basic state becomes linearly unstable. In RBC the first destabilizing modes to acquire a positive growth rate as ΔT increases beyond ΔT_c are characterized by the critical wavenumber q_c. Since q_c is non-zero, these modes give rise to spatially varying convection patterns.

RBC usually is studied in the Oberbeck–Boussinesq (OB) approximation (Oberbeck 1879; Boussinesq 1903). There the temperature dependences of the thermal diffusivity κ and the kinematic viscosity ν are neglected. In addition, the density (which provides the buoyancy force crucial for RBC) is assumed to vary linearly as a function of T between T_b and T_t, implying that the thermal expansion coefficient α is constant. In this approximation the bifurcation to convection rolls at $\Delta T = \Delta T_{c,OB}$ is stationary and continuous, i.e. supercritical (Schlüter, Lortz & Busse 1965). Thus the onset of convection $\Delta T_{c,exp}$ observed in experiments is expected to agree with $\Delta T_{c,OB}$ within the experimental resolution.

There is a sizable literature devoted to the theoretical study of so called non-Oberbeck–Boussinesq (NOB) effects that occur when the assumptions of the OB approximation break down. An important study of weak NOB corrections near the onset of convection, i.e. for $\Delta T \approx \Delta T_c$, was carried out by Busse (1967). He considered the temperature variations of κ, ν and α to be small and kept them in the leading-order linear approximation. As a result the standard supercritical bifurcation to rolls in the OB system is replaced by a hysteretic transcritical bifurcation to a stationary hexagonal pattern, while ΔT_c and q_c remain unchanged. As a consequence, in experiments the onset of convection in the form of hexagons at $\Delta T_{c,exp}$ slightly below ΔT_c may occur in the presence of finite-amplitude perturbations, inhomogeneities near boundaries or thermally induced fluctuations.

The various implications of NOB conditions were confirmed to a large extent by several experiments (Hoard, Robertson & Acrivos 1970; Ahlers 1980; Walden & Ahlers 1981; Ciliberto, Pampaloni & Perez-Garcia 1988; Ciliberto *et al.* 1990; Perez-Garcia, Pampaloni & Ciliberto 1990; Bodenschatz *et al.* 1991, 1992; Pampaloni *et al.* 1992). In the present paper we address, both experimentally and theoretically, several new aspects of how NOB effects manifest themselves when the assumption of weak temperature variations of the fluid properties in the sense of Busse ceases to be valid. This situation prevails, for instance, in a gas near its gas–liquid critical point, even for $\Delta T \approx \Delta T_c$, and this is the system studied experimentally in the present project (for earlier experiments, see e.g. Assenheimer & Steinberg 1993; Roy & Steinberg 2002).

Our theoretical analysis is based exclusively on a deterministic hydrodynamic description of the system. Although thermally induced fluctuations (Swift & Hohenberg 1977; Hohenberg & Swift 1992) (which are neglected in the deterministic equations) become stronger near the critical point and are readily observed below the onset of convection (Oh & Ahlers 2003), we found no indications that the influence of thermal noise had to be included in the comparison with the experimental results for the bifurcation points and patterns reported in this paper. In any case, an analysis of NOB effects using fluctuating hydrodynamics (Landau & Lifshitz 1987) would be a highly demanding task.

For completeness we mention that a significant effort was devoted recently also to the study of NOB effects well above the onset of convection in a regime where the fluid flow is highly turbulent (Wu & Libchaber 1991; Zhang, Childress & Libchaber 1997, 1999; Ahlers *et al.* 2006, 2007; Sugiyama *et al.* 2007; Ahlers *et al.* 2008).

In order to illustrate the issues that arise in near-critical fluids, we describe their properties briefly in § 2 and show qualitatively that the NOB effects can lead to a considerable increase of ΔT_c beyond the value for the OB case. There we show also that the 'classical' signature of NOB convection, the bifurcation to hexagons, may remain unobservable for those systems. It should be stressed that we used very thin fluid layers, of thickness $d \approx 50$ μm, in the present work. In that case the stabilizing compression of the fluid under its own weight near the bottom of the sample is completely negligible. However, this mechanism can be important near the critical point for fluid layers with thicknesses of the order of 1 cm or more; in those cases it can also lead to a considerable increase of ΔT_c compared to the OB value (see e.g. Ashkenazi & Steinberg 1999; Kogan & Meyer 2001).

In § 3 we describe briefly the experimental set-up. Section 4 is devoted to a detailed discussion of the experimental results. In § 5 we provide the background for theoretical analysis of NOB effects in the present system and discuss the resulting shifts of ΔT_c. Section 6 is devoted to the weakly nonlinear regime. In this context also the theoretical results of Busse were re-examined. This led to adjustments of some of the numerical values of coefficients given by Busse (1967). Section 7 contains some concluding remarks, and finally some technical details can be found in two appendices.

2. Qualitative features of RBC in 'near-critical' fluids

The working fluid used in the experiment was sulfur hexafluoride (SF_6) with temperatures T_t, T_b slightly above the critical temperature $T^* = 318.72$ K and at pressures just above the critical pressure $P^* = 37.55$ bars. Under those conditions the fluid density ρ was close to the critical density $\rho^* = 742$ kg m^{-3}. The equation of state of SF_6 was taken from the work of Wyczalkowska & Sengers (1999). In figure 1 we show the phase diagram in the temperature–density plane. The dashed line denotes the co-existence curve of liquid and vapour and the dotted lines the critical isochore (ρ^*) and isotherm (T^*).

In the present paper we report measurements on the three isobars $P_{is} = 38.09,\ 38.33,$ and 39.59 bars illustrated by the solid lines in figure 1. Some of the results have been reported briefly in previous publications (Ahlers & Oh 2003; Oh & Ahlers 2003; Oh *et al.* 2004; Ahlers 2006). The pairs of symbols (open circles, solid circles, stars) on each isobar indicate the bottom temperatures T_b (left) and top temperatures T_t (right) at the experimentally observed onset of convection, i.e. for $\Delta T = T_b - T_t = \Delta T_{c,exp}$. Note that the small temperature differences involved correspond nevertheless to large temperature gradients because of the small thickness $d \approx 50$ μm of the fluid layer used in the experiments. In three experimental runs (indicated as E-I, E-II, E-III in the following) the average temperature $T_m = (T_b + T_t)/2$ was chosen so that the condition $\rho(T_m) = \rho^*$ was fulfilled to high accuracy. Two additional runs (indicated as E-IV, E-V in the following), on the isobar $P_{is} = 39.59$ bars, were made with $\rho(T_m) < \rho^*$. For these the temperature extrema of the fluid at onset are shown as solid circles and stars. The experimental parameters for the five runs are listed in table 1. Only the total critical temperature $\Delta T_{c,tot}$ across the whole convection cell including the confining plates is measured. The critical temperature difference $\Delta T_{c,exp}$ across the fluid layer is

Experiment	E-I	E-II	E-III	E-IV	E-V
P_{is} (bars)	38.091	38.326	39.587	39.587	39.587
T_m (°C)	46.219	46.500	48.002	48.097	48.296
$(T_m - T^*)/T^*$	0.0020	0.0029	0.0076	0.0079	0.0086
$(\rho_m - \rho^*)/\rho^*$	−0.0005	−0.0003	0.0000	−0.0478	−0.1212
d (μm)	34.3	34.3	59	59	59
$\Delta T_{c,tot}$(K)	0.304	0.930	0.616	0.670	1.023
Pattern	R	R	R	$H + R$	H

TABLE 1. Parameters for and results from the five experimental runs E-I–E-V. The pressure P_{is}, mean temperature T_m, relative distances of T_m and ρ_m from the critical values T^* and ρ^*, cell thickness d, experimental critical temperature difference $\Delta T_{c,tot}$ across the whole convection cell including the top and bottom plates, and the observed type of pattern (R: rolls, H: hexagons) are given.

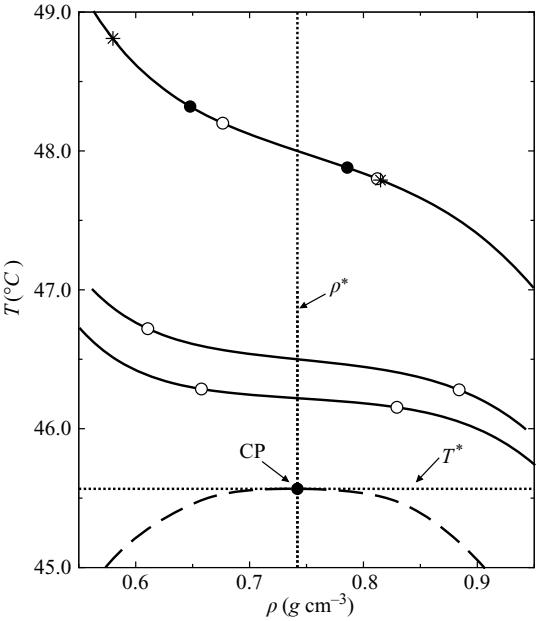

FIGURE 1. Temperature–density plane near the critical point (CP) of SF_6. Dashed line: coexistence curve of liquid and vapour. Dotted lines: critical isochore (ρ^*) and isotherm (T^*). Solid lines from bottom to top: the isobars $P_{is} = 38.09$, 38.33 and 39.59 bars used in the experiment. Each symbol pair on the solid lines represents the highest and lowest temperature at the onset of convection for a given mean sample temperature T_m. The open circles are for runs with $\rho(T_m, P_{is}) = \rho^*$. The solid circles and stars on the isobar $P_{is} = 39.59$ bars correspond to $T_m = 48.10\,°C$ and 48.30 °C, respectively.

then calculated as $\Delta T_{c,exp} = r\Delta T_{c,tot}$, where r is an estimate of the ratio of the thermal resistance of the fluid layer to the total thermal resistance (for details see § 3).

As usual, we introduce the Rayleigh number R as a non-dimensional measure of the applied temperature difference ΔT:

$$R \equiv \Delta T / T_s = \frac{\alpha_m C_{p,m} \rho_m^2 g d^3}{\lambda_m \eta_m} \Delta T. \tag{2.1}$$

It involves the temperature scale T_s defined as

$$T_s \equiv \frac{\kappa_m \nu_m}{\alpha_m g d^3} = \frac{\lambda_m \eta_m}{\alpha_m C_{p,m} \rho_m^2 g d^3}, \tag{2.2}$$

where g is the gravitational acceleration. The subscript 'm' denotes that the material constants are evaluated at the temperature $T = T_m$. In the second term on the r.h.s. of (2.2) we introduced the shear viscosity $\eta = \nu\rho$ and the thermal conductivity $\lambda = C_p \rho \kappa$, where C_p denotes the heat capacity at constant pressure. Note that in the present work T_b and T_t always were varied at constant T_m. In the framework of the OB theory the critical temperature difference $\Delta T_{c,OB}$ is given by

$$\Delta T_{c,OB} = R_{c,OB} T_s \quad \text{with } R_{c,OB} = 1707.8. \tag{2.3}$$

According to (2.3) small values of T_s lead to small values of $\Delta T_{c,OB}$. As realized, for instance, by Assenheimer & Steinberg (1993), this situation prevails near a liquid–gas critical point, since both α and C_p diverge strongly as T^* is approached from above. The thermal conductivity λ diverges less strongly than α and C_p, and η remains finite. Thus, at constant d the temperature scale T_s (2.2), and thus also $\Delta T_{c,OB}$ (2.3), will vanish at T^*. For completeness, we mention that upon approaching the critical point the isothermal compressibility

$$k_T = \rho^{-1} \frac{\partial \rho}{\partial p}\bigg|_T = \alpha \frac{\partial T}{\partial p}\bigg|_\rho \tag{2.4}$$

(p denotes the pressure) diverges as well. However, we will demonstrate in § 5.1 that the ensuing strong pressure dependence of the density is not important for the present case.

For the evaluation of $\Delta T_{c,OB}$ according to (2.2), (2.3) we need, besides $\alpha(T)$, $\rho(T)$, and $C_p(T)$ (Wyczalkowska & Sengers 1999), the shear viscosity $\eta(T)$ and the thermal conductivity $\lambda(T)$. For $\eta(T)$ we used a fit of a piecewise smooth function to data from Hoogland, van den Berg & Trappeniers (1985) and from Strehlow & Vogel (1989). This approach neglects a small anomaly of the viscosity at the critical point. For $\lambda(T)$ we used a smooth-function fit to a variety of conductivity data in the literature (Lis & Kellard 1965; Lim *et al.* 1971; Swinney & Henry 1973; Kestin & Imaishi 1985). These data define λ quite well along the critical isochore, but are less definitive away from $\rho = \rho^*$ (i.e. for the runs E-IV and E-V). In table 2 we present the material parameters at $T = T_m$ for our five experimental runs together with the Prandtl number $\sigma = \nu_m/\kappa_m = C_{p,m}\eta_m/\lambda_m$. Note that σ diverges as well as $T \to T^*$. Furthermore we included the data for $r = \Delta T_{c,exp}/\Delta T_{c,tot}$ which depend on d/λ_m (see § 3).

In the first row of table 3 we give the experimental values $\Delta T_{c,exp}$ of the critical temperature differences across the fluid. With the use of the material parameters in table 2 and (2.3) one obtains the OB critical temperature differences $\Delta T_{c,OB}$ for the five experimental runs. They are listed in the second row of table 3. In the third row of that table we show the corresponding experimental critical temperature differences normalized by $\Delta T_{c,OB}$, i.e. $\delta T_{c,exp} = \Delta T_{c,exp}/\Delta T_{c,OB}$. The following two rows present our theoretical NOB results, which will be discussed in detail below in § 5. The fourth row contains $\delta T_{c,theor} = \Delta T_c/\Delta T_{c,OB}$, where ΔT_c was determined from the exact linear stability analysis of the basic state (5.23). Finally, the fifth row shows an 'analytical' approximation to the NOB critical temperature difference in the form $\delta T_{c,app} = \Delta T_{c,app}/\Delta T_{c,OB}$, where $\Delta T_{c,app}$ is given by (5.28).

Although the values of $\Delta T_{c,OB}$ shown in table 3 are of the same order of magnitude as the experimental $\Delta T_{c,exp}$, the latter turn out to be systematically larger than $\Delta T_{c,OB}$

Experiment	E-I	E-II	E-III	E-IV	E-V
α_m (1/K)	2.459	1.590	0.498	0.472	0.339
$C_{P,m}$ (kJ kg^{-1} K^{-1})	89.52	58.35	19.07	18.12	13.28
ρ_m (kg m^{-3})	741.6	741.3	742.0	708.4	652.5
$10^5 k_{T,m}$ (m^2 N^{-1})	2.936	1.900	0.593	0.586	0.454
$10^2 \lambda_m$ (W m^{-1} K^{-1})	7.53	6.897	5.774	5.70	5.521
$10^5 \eta_m$ (kg m^{-1} s^{-1})	4.023	4.024	4.040	3.820	3.486
σ	47.81	34.04	13.34	12.14	8.33
r	0.451	0.473	0.647	0.652	0.658

TABLE 2. Material parameters at $T = T_m$ for the experiments E-I–E-V together with the Prandtl number σ and $r = \Delta T_{c,exp}/\Delta T_{c,tot}$ (see § 3).

Experiment	E-I	E-II	E-III	E-IV	E-V
$\Delta T_{c,exp}$(K)	0.131	0.440	0.398	0.437	0.673
$\Delta T_{c,OB}$ (K)	0.1082	0.2352	0.3787	0.4313	0.8529
$\delta T_{c,exp}$	1.206	1.87	1.053	1.013	0.789
δT_c	1.304	1.82	1.06	1.032	0.879
$\delta T_{c,app}$	1.35	1.92	1.05	1.04	0.92

TABLE 3. Experimental and theoretical values of the critical temperature differences. The first row gives the experimental estimate of the critical temperature difference $\Delta T_{c,exp} = r\Delta T_{c,tot}$ across the fluid. Here r is from table 2 and $\Delta T_{c,tot}$ is from table 1. The second row contains the OB values $\Delta T_{c,OB}$ given by (2.2) and (2.3). The third, fourth and fifth rows give critical temperature differences normalized by the OB value $\Delta T_{c,OB}$: $\delta T_{c,exp} = \Delta T_{c,exp}/\Delta T_{c,OB}$, $\delta T_c = \Delta T_c/\Delta T_{c,OB}$ from (5.23), and $\delta T_{c,app} = \Delta T_{c,app}/\Delta T_{c,OB}$ from (5.28)

for the runs E-I, E-II, E-III, while $\Delta T_{c,exp} < \Delta T_{c,OB}$ for E-V. To understand this feature we realize that the vicinity of the critical point is characterized not only by large values of $C_{p,m}$ and α_m, but also by their strong temperature dependences along an isobar. This is demonstrated in figure 2. There we show C_p for the experiment E-I as function of the reduced temperature

$$\tilde{\delta}(T) = (T - T_m)/\Delta T_{c,OB} \tag{2.5}$$

as a representative example. One sees that C_p decreases by almost a factor of 2.5 from its maximum at $\tilde{\delta} = 0$ (i.e. at $T = T_m$) as T approaches T_b or T_t. The temperature variation of α is comparable while the temperature dependences of the other material parameters are much weaker (see figure 11).

To capture approximately the general behaviour of the NOB critical temperature difference, it seems reasonable to replace T_s in (2.3) by a suitable average $\overline{T}_s$ over the temperature interval $T_b \leqslant T \leqslant T_t$. A reasonable choice for $\overline{T}_s$ would be (2.2), but with $C_{p,m}$ and α_m replaced by their corresponding averages $\overline{C}_p$ and $\overline{\alpha}$. Inspection of figure 2, as well as of figure 11, illustrates that $\overline{\alpha} < \alpha_m$ and $\overline{C}_p < C_{p,m}$ for the experiments E-I–E-III. Thus $\overline{T}_s > T_s$ and $\Delta T_c/\Delta T_{c,OB} = \overline{T}_s/T_s > 1$. This estimate is confirmed by the experimental and the exact theoretical critical temperature differences presented in table 3. In contrast, we expect $\Delta T_c/\Delta T_{c,OB} < 1$ for E-V since $\overline{\alpha}, \overline{C}_{p,m} < \alpha_m, C_{p,m}$. This is confirmed as well in table 3. The approach described above will be put on a more sound theoretical foundation in § 5. Considering the resulting values for $\Delta T_{c,app}/\Delta T_{c,OB}$ (see (5.28)) in table 3, the approximation scheme works quite

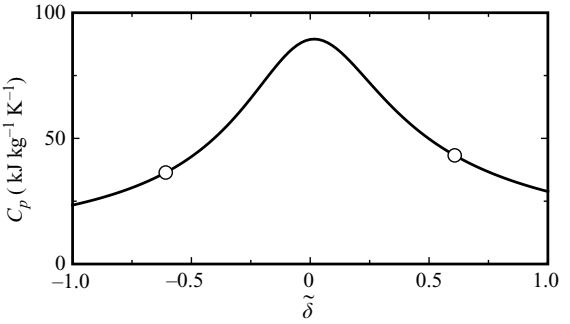

FIGURE 2. The heat capacity at constant pressure C_P as a function of $\tilde{\delta} = (T - T_m)/\Delta T_{c,OB}$ for $P_{is} = 38.09$ bars, and for $T_m = 46.22\,^{\circ}\mathrm{C}$ chosen so that $\rho(T_m) = \rho^*$. The two open circles correspond to the values $T_m \pm \Delta T_{c,exp}/2$ for the experimental run E-I.

well. Thus it is apparent that the values of $\overline{C}_p/C_{p,m}$ and $\overline{\alpha}/\alpha_m$, which become 1 in the OB case, play a crucial role in determining the shifts of ΔT_c in the NOB case.

It is important to realize that the averages $\overline{C}_p$ and $\overline{\alpha}$ reflect only the contributions to $C_p(\tilde{\delta})$ and $\alpha(\tilde{\delta})$ which are even in $\tilde{\delta}$. If only these even-in-$\tilde{\delta}$ terms are kept for the other material parameters as well, the hydrodynamic equations obey the Boussinesq symmetry, i.e. they are invariant under the reflection $z \to -z$ at the horizontal midplane of the cell.

The odd-in-$\tilde{\delta}$ contributions to the material parameters, on the other hand, which break the Boussinesq symmetry, will not modify ΔT_c significantly, but are responsible for the 'classical' NOB effects: In their presence, the nature of the bifurcation and the convection planform near onset change qualitatively. Instead of a bifurcation to rolls, a transcritical bifurcation to a hexagonal pattern generally takes place. Associated with that bifurcation is a saddle node located at $\epsilon = \epsilon_a < 0$ below which the hexagons cease to exist and only the conduction state is stable.

Here and in the following we use

$$\epsilon = \Delta T/\Delta T_c - 1 \tag{2.6}$$

as the conventional reduced distance from onset. With increasing ϵ a point of marginal stability of rolls is reached at $\epsilon_r > 0$. Beyond ϵ_r both rolls and hexagons can exist until $\epsilon_b > \epsilon_r$ where hexagons become unstable (for more details, see § 6). Inspection of figure 2, as well as of figure 11, shows that the odd-in-$\tilde{\delta}$ terms in the material parameters are very small when T_m is chosen so that $\rho(T_m, P_{is}) = \rho^*$. Thus within our experimental resolution only rolls should be seen near onset for the three runs E-I, E-II and E-III. This is indeed confirmed by the experiments (see § 4) and has been documented already in the last row of table 1. The situation is different for the two runs E-IV and E-V with $\rho(T_m, P_{is}) < \rho^*$. Here the corresponding odd-in-$\tilde{\delta}$ terms become considerably larger, and indeed we observe hexagons in the experiments.

The classical NOB scenario was quantified by Busse (1967) in a pioneering paper. For simplicity he first neglected the even-in-$\tilde{\delta}$ corrections to α, C_p, etc. completely and performed a perturbative analysis with respect to the odd corrections to linear order

in $\tilde{\delta}$. He thus used the following representation of the material parameters:

$$\hat{\rho}(T) \equiv \frac{\rho(T)}{\rho_m} = 1 - \gamma_0\left(\tilde{\delta} + \gamma_1\tilde{\delta}^2\right), \tag{2.7a}$$

$$\hat{\nu}(T) \equiv \frac{\nu(T)}{\nu_m} = 1 + \gamma_2\tilde{\delta}, \tag{2.7b}$$

$$\hat{\lambda}(T) \equiv \frac{\lambda(T)}{\lambda_m} = 1 + \gamma_3\tilde{\delta}, \tag{2.7c}$$

$$\hat{C}_p(T) \equiv \frac{C_p(T)}{C_{p,m}} = 1 + \gamma_4\tilde{\delta}. \tag{2.7d}$$

From (2.7*a*) the thermal expansion coefficient α in this approximation is given by

$$\alpha(T) = -\frac{1}{\rho(T)}\frac{\partial\rho(T)}{\partial T} = \frac{\gamma_0}{\Delta T_{c,OB}}(1 + (\gamma_0 + 2\gamma_1)\tilde{\delta}), \tag{2.8}$$

and consequently $\alpha_m = \gamma_0/\Delta T_{c,OB}$. Since we have access to the temperature dependences of the material parameters, the γ_i are available as well.

The strength of the classical NOB effects usually is characterized by the Busse parameter

$$Q = \sum_{i=1}^{4} \gamma_i \mathscr{P}_i. \tag{2.9}$$

The coefficients $\mathscr{P}_i$ are linear functions of σ^{-1} and were calculated by Busse in the limit $\sigma \to \infty$. Except for a calculational error in $\mathscr{P}_3$, they were confirmed by our own calculations (for more details see § 6.1). We obtained the following expressions (first given by Tschammer 1996):

$$\begin{aligned} &\mathscr{P}_0 = 2.676 - 0.361/\sigma \ , \mathscr{P}_1 = -6.631 - 0.772/\sigma, \\ &\mathscr{P}_2 = 2.765 \ , \mathscr{P}_3 = 9.54, \\ &\mathscr{P}_4 = -6.225 + 0.3857/\sigma. \end{aligned} \tag{2.10}$$

Busse obtained expressions for ϵ_a, ϵ_r, and ϵ_b; all of them are proportional to Q^2 (see § 6.1 and Appendix A). To a good approximation the hexagonal patterns can be described by three coupled Ginzburg–Landau equations (see e.g. § 6) which have a potential. One can then define (see Bodenschatz *et al.* 1991 and references therein) a point ϵ_T with $\epsilon_a < \epsilon_T < 0$ where the potentials of the pure conduction state and the hexagons are equal. In a sample with a gradient of ϵ, for instance because of a small spatial variation of the spacing d over the cell, the conduction state and the hexagonal pattern may be able to co-exist in different spatial regions. In that case one would expect a front between them at a location where $\epsilon = \epsilon_T$. Similarly, at a point $\epsilon_r < \epsilon_{T'} < \epsilon_b$ the potentials of rolls and of hexagons are equal, and in principle a co-existence of rolls and hexagons could occur in a non-uniform sample. In the presence of localized inhomogeneities, such as the sidewalls or even very small local imperfections, a transition between patterns can be induced at ϵ_T or $\epsilon_{T'}$ instead of at the points of marginal stability.

To give a first impression of the magnitude of the classical NOB effects, we listed in table 4 the coefficients γ_i (2.7), the values of Q (2.9), and the values of the stability limits based on the explicit expressions in Appendix A, for each of the five experimental runs. We obtained the values of the γ_i by using the derivative of the

Experiment	E-I	E-II	E-III	E-IV	E-V
γ_0	0.2660	0.3736	0.1887	0.2031	0.2881
γ_1	−0.0633	−0.1131	−0.0751	−0.3520	−0.9118
γ_2	−0.0639	−0.0892	−0.0444	−0.0349	−0.0192
γ_3	−0.0510	−0.0692	−0.0271	−0.1106	−0.0791
γ_4	0.2012	0.2111	0.0396	−0.4705	−1.4458
Q	−0.78	−0.47	0.38	4.66	15.01
$10^3\epsilon_a$	−0.100	−0.036	−0.025	−3.67	−38.1
$10^3\epsilon_r$	8.77	3.14	1.95	298	(3030)
$10^3\epsilon_{T'}$	12.09	4.33	2.69	411.8	(4180)
$10^3\epsilon_b$	29.99	10.76	6.68	(1024)	(10400)

TABLE 4. The coefficients γ_i (2.7), the Busse parameter Q (2.9), and the stability limits ϵ_a, ϵ_r, ϵ'_T, and ϵ_b based on the classical NOB expressions shown in § 6.1 and Appendix A. The data in parentheses have relatively large uncertainties, as discussed in § 4.1.

material parameters (2.7) with respect to $\tilde{\delta}$ at $\tilde{\delta}=0$. In much of the literature it has been customary to calculate γ_i via a finite difference such as $\gamma_4=\hat{C}_p(T_t)-\hat{C}_p(T_b)$, using the material parameters at the top and the bottom of the layer. This procedure is reliable if the temperature dependences of the material parameters are well described by the approximations given in (2.7) over the whole temperature range, but is not really justified in our case of strong temperature variations.

Qualitatively, the patterns observed near onset (see table 1) are well described by the parameters in table 4: The small values of Q for the runs E-I, E-II and E-III, which led to small values of $\epsilon_r, \epsilon_b \sim Q^2$, are consistent with the fact that only rolls are observed in the experiments. For E-IV we obtained a much larger Q value, and indeed we were able to observe the hysteretic transition to hexagons and the subsequent transition to rolls with increasing ϵ. Consistent with the very large Q value for E-V, which implies $\epsilon_r > 1$, a transition from hexagons to rolls was not reached in the experiment. The experimental details and a comparison with the theory are presented in § 4.

3. Apparatus and procedures

The measurements were made with sulfur hexafluoride (SF_6) near but slightly above its gas–liquid critical point. The apparatus and experimental procedures were described in detail by de Bruyn *et al.* (1996), and the particular modifications required for working near the critical point were discussed by Oh *et al.* (2004). We mention briefly that the entire sample was surrounded along the sides and bottom by a can that was maintained at the temperature of the top-plate cooling water. The can contained a volume of fluid much larger than that of the sample. There was optical access to the sample from the top. The pressure was held constant to approximately ± 1 mbar by adjusting the temperature of an external gas volume that was connected to the can by a capillary. This adjustment was done in response to the readout of a pressure gauge through a computer-controlled feedback loop.

The bottom plate of the convection cell was an optically flat sapphire of thickness 0.318 cm on top of an aluminum plate. A metal-film heater glued to the bottom of the aluminum plate provided the heat current. A thin silver film was evaporated on the top surface of the sapphire to provide a mirror for the shadowgraphy. The top plate was also an optically flat sapphire of 0.318 cm thickness. A temperature-controlled

water bath cooled the top sapphire; it was maintained at or very near the sample pressure so as to minimize sample distortion due to a pressure difference across the top sapphire. At the top of the water bath optical access was available through a non-crystalline quartz window.

The cell spacing was fixed by a porous paper sidewall with an inner (outer) diameter of 2.5 (3.5) cm. Since the top sapphire was supported along its perimeter which had a diameter of 10 cm (i.e. considerably larger than the cell wall), the force exerted on the cell top by the bottom plate and the wall caused a slight upward bowing of the initially flat top. Over the entire sample diameter this yielded a radial cell-spacing variation corresponding to about one circular fringe when illuminated with an expanded parallel He–Ne laser beam. This variation of the thickness by about 0.3 μm assured that convection would start in the cell centre, rather than being nucleated inhomogeneously near the cell wall. Assuming a parabolic radial profile for the cell spacing, we estimate that the spacing was uniform to much better than 0.1 % over the 1.9×1.9 mm^2 area near the cell centre. The actual sample thickness was measured interferometrically (de Bruyn *et al.* 1996) and found to be 34.3 μm for some of the measurements and 59 μm for the others.

Patterns were visualized by the shadowgraph method (de Bruyn *et al.* 1996) by recording the pictures in the uniform central region mentioned above. At each pressure P_{is} and mean temperature T_m a sequence of images with $\Delta T = 0$ was averaged and used as a reference image. All other images were then divided by this reference. Fourier transforms of the ratios were obtained, and the integrals of the squares of their moduli yielded the total power in Fourier space, equivalent to the variance in real space. The reference-divided image was re-scaled in proportion to its own variance to yield a rendering of the patterns over a suitable grey-scale range.

In experiments on RBC with very thin samples it is difficult to determine the temperature drop ΔT across the fluid layer and the mean temperature T_m of the fluid with high accuracy. Because of the small sample thickness the thermal resistance of the sample was comparable to those of the top and bottom confining plates even though these plates had much higher thermal conductivities. Thus an imposed $\Delta T_{tot} = (T_{BP} - T_{bath})$ (T_{BP} and T_{bath} are the imposed bottom-plate and bath temperatures, respectively) is the sum of the temperature differences across the bottom aluminum plate ΔT_{Al}, across the boundary between the aluminum plate and the bottom sapphire ΔT_{b1}, across the bottom sapphire ΔT_{sb}, across the sample ΔT, across the top sapphire ΔT_{st} and across a boundary layer above the top sapphire in the water bath ΔT_{b2}. From estimates of the thermal resistances of these sections we determined the ratio $r \equiv \Delta T / \Delta T_{tot}$. Although the top- and bottom-plate resistances were essentially constant over the narrow temperature range of the experiments, the sample resistance changed from one run to another because the sample conductivity varied and because the sample spacing was not always the same. The values of r for $\Delta T_{tot} = \Delta T_{c,tot}$ are given in table 2 for each experimental run. By definition they yield the critical temperature difference $\Delta T_{c,exp}$ across the fluid layer from the measured $\Delta T_{c,tot}$. Near onset they also give the temperature differences ΔT across the sample from the total differences ΔT_{tot} with sufficient accuracy. The systematic errors in ΔT due to uncertainties of r are difficult to estimate, but are probably a few percent on the critical isochore and larger away from it.

The small thermal resistance of the sample also required a special procedure to assure that the sample was indeed at or near the temperature corresponding to ρ^* or a known temperature increment away from it. Before a run on a given isobar was started, a fixed ΔT_{tot} sufficiently small for ΔT to be below the onset value of

convection was imposed. Measurements of the power of shadowgraph images of the fluctuations as a function of the mean temperature $T_{m,tot} = (T_{BP} + T_{bath})/2$ then were made. Thereafter T_{bath} and T_{BP} were adjusted so as to hold the mean sample temperature T_m constant at the value of maximum fluctuation power throughout a run in which the temperature difference ΔT was changed in steps. In practice it turned out that the thermal resistances of the top plate and the composite bottom plate were dominated by the sapphires and thus were nearly equal. As a consequence a constant $T_{m,tot}$ was nearly equivalent to a constant T_m. We note that the maximum of the fluctuation power does not necessarily occur precisely on the critical isochore; but the deviation is small.

4. Experimental results

This section is devoted to a detailed discussion of the five experimental runs listed in table 1. We give the results for $\Delta T_{c,exp}$ (see table 3), show the patterns that are observed near onset, provide data for the intensity of these patterns and examine how these data compare with the theoretical results.

4.1. *General remarks about the comparison with theory*

As already discussed in § 2, we find considerable shifts of $\Delta T_{c,exp}$ relative to $\Delta T_{c,OB}$ (see table 3). These shifts are described satisfactorily by the complete linear stability analysis presented in § 5. This analysis can be performed only numerically. However, the relevant physical mechanism could be elucidated in terms of a quasi-analytical approach.

We demonstrated already in § 2 that only the Busse parameter Q is needed to explain qualitatively the general trend of the observed patterns in the nonlinear regime near onset. This trend could be understood in the framework of the classical NOB analysis (Busse 1967; see the predictions given in table 4). However, a quantitative understanding of the experimentally observed stability limits is not possible within the framework of this analysis for several reasons. First, this theory utilizes a linear material-property approximation (2.7). This is in conflict with the strong nonlinear temperature variations (see e.g. figure 2) in the present case. These variations are responsible for the ΔT_c shifts. In addition, the classical NOB effects are assumed to be small, which implies small $\gamma_i, i = 1, \ldots, 4$ in (2.7). This stands in contrast to the large γ_i values for E-IV and E-V. However, keeping the full temperature dependences of the material parameters only leads to a partial improvement of the stability limits (compare the entries in tables 4 and 8) because even our complete analysis is based on a weakly nonlinear theory, which in general is justified only at small $|\epsilon|$. Thus, the large values of ϵ_r and ϵ_b of order 1 in tables 4 and 8 are not trustworthy.

Last but not least, for the present near-critical fluids all theoretical estimates, in particular the stability limits, depend sensitively on the average temperature T_m, the pressure P_{is}, and the precise knowledge of the temperature dependence of the material parameters. As mentioned already in § 2, especially the uncertainties of λ for the experimental runs E-IV and E-V lead to relatively large uncertainties of the derived quantities. Even for runs E-I–E-III, where the properties are relatively well established, we find that very small changes within the small experimental uncertainties of P_{is} and/or T_m can have a significant effect on the material parameters. As a consequence of the combined effect of all the uncertainties discussed before, the agreement between theory and experiment, in particular with respect to the stability limits, is expected to be only semiquantitative in the best cases.

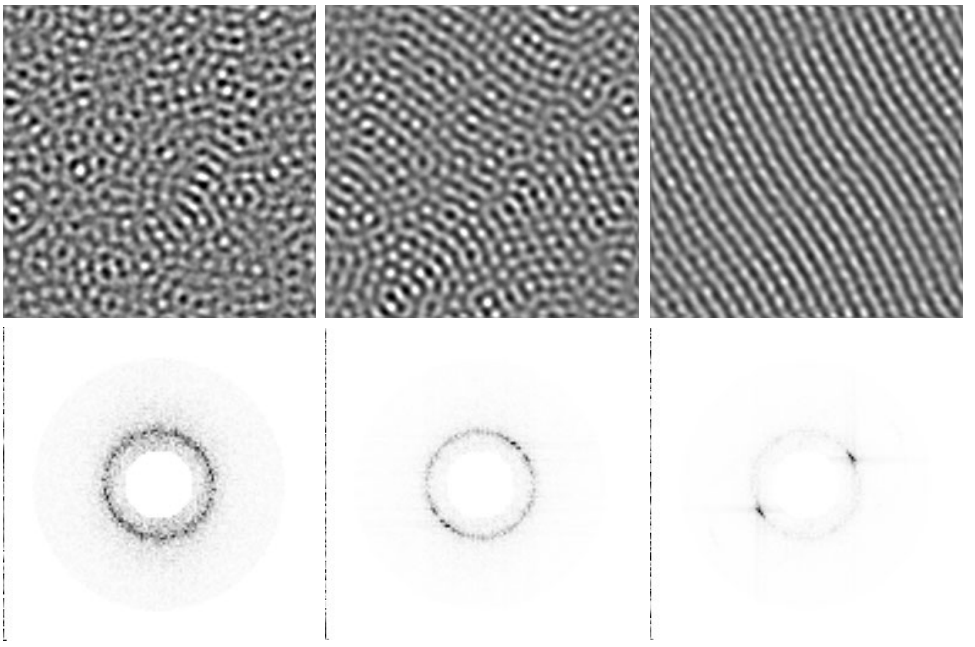

FIGURE 3. Shadowgraph images (top row) and the moduli of their Fourier transforms (bottom row) for (a–c) $\Delta T = 0.3972$, 0.3985 and 0.3998 K at $P_{is} = 39.59$ bars and $T_m = 48.00$ K°C (E-III). Each image covers an area of 0.96×0.96 mm^2. The centre of the Fourier transform was removed to eliminate an instrumental noise peak near the origin.

4.2. *Near-OB convection on the critical isochore*

The NOB effects are expected to be smallest at the highest pressure with the maximal value of $T_m - T^*$. Thus, the isobar $P_{is} = 39.587$ bars was used to study a case that conforms fairly well to the Boussinesq approximation. The mean temperature was adjusted to be 48.000 °C (on our temperature scale) which yielded a maximum of the shadowgraph intensity below onset and thus was presumed to correspond approximately to $\rho(T_m) = \rho^*$. The experimentally found onset for this case (E-III) is illustrated by the open circles on the top solid line in figure 1.

Figure 3 shows three shadowgraph images of the patterns near the centre of the sample and the moduli of their Fourier transforms. In this experiment ΔT was decreased in small steps from larger values where there was a well-developed roll pattern, with an equilibration time at each step of about 160 min. We note that the rolls above onset are influenced significantly by thermal noise. The response to the noise yields the superimposed small-scale structure that leads to a remnant faint ring in Fourier space, and results in the long-wavelength undulations of the rolls. Below onset, at $\Delta T = 0.3972$ K (left image), one sees only random fluctuations driven by the Brownian motion of the molecules. This leads to a nearly uniform ring in Fourier space, reflecting the rotational invariance of the RBC system. The middle image, at $\Delta T = 0.3985$ K, already reveals some organization in a preferred direction, although the fluctuations still dominate. Finally, in the right image at $\Delta T = 0.3998$ K, a clear roll structure is evident and gives two well-defined spots in Fourier space. As discussed by Oh & Ahlers (2003), even in this last case above onset fluctuations still exist and lead to a background ring in the Fourier transform modulus. As expected from the relevant entries in table 8 (which are of the same order of magnitude as the

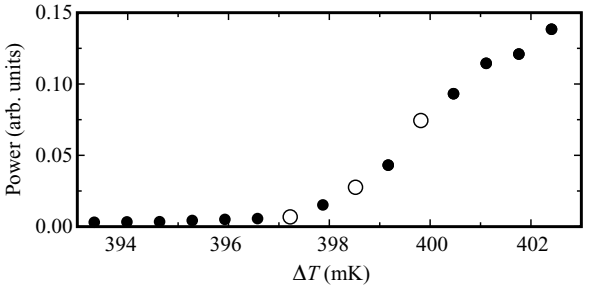

FIGURE 4. The total shadowgraph power as a function of ΔT for $P_{is} = 39.59$ bars and $T_m = 48.00\,^{\circ}\mathrm{C}$ (E-III). The open circles correspond to the images shown in figure 3.

approximate analytical ones in table 2), none of these images show any evidence of a hexagonal structure that would be expected if classical NOB effects had a noticeable influence. This is particularly clear by inspection of the Fourier transforms in figure 3 which reveal the formation of a single pair of peaks, characteristic for rolls, as ΔT is increased. In figure 4 we show the total power obtained from integrating the square of the Fourier transform modulus after removal of small experimental contributions near the centre. The open circles correspond to the images shown in figure 3. One sees a well-defined onset of convection, and a continuous increase from zero of the power beyond onset.

On the basis of the experimental data in figures 3 and 4, we chose $\Delta T_{c,exp} = 0.398$ K (listed in table 3). Within ± 0.001 K, the same value of $\Delta T_{c,exp}$ was found in another experimental run where ΔT was increased. This value is about 5 % higher than the corresponding Boussinesq value $\Delta T_{c,OB} = 0.379$ K (see table 3) obtained from (2.2), (2.3) and the material properties at T_m (see table 2). We consider this difference to be larger than the uncertainties due to the fluid properties. In fact there is very good agreement with the increase of the theoretical ΔT_c by about 6 % compared to $\Delta T_{c,OB}$.

4.3. *Classical NOB convection away from the critical isochore*

Moving away from the critical isochore at the same pressure $P_{is} = 39.59$ bars, the onset of convection changes qualitatively. For the run E-IV ($T_m = 48.100\,^{\circ}\mathrm{C}$) the approximate classical NOB theory (see table 4) yields the estimate $Q = 4.66$, considerably larger than at $T_m = 48.00\,^{\circ}\mathrm{C}$ in §4.2. The very good agreement of the approximate stability limits (table 4) and the fully numerical ones (table 8) is reassuring. A sequence of images for E-IV is shown in figure 5. This experiment was done by changing ΔT in steps of 0.6 mK, and equilibrating at each step for 40 min before taking the image. From bottom to top one sees first only fluctuations, then the formation of an island of hexagons, then a spreading of the area occupied by the hexagons. The hexagons are of course the hallmark of the transition to convection in a NOB system. The initial formation of the small island is attributable to the small inhomogeneity of the sample thickness (see §3). No hysteresis was detectable at onset. Given the small value of the theoretical $\epsilon_a \simeq -3.2 \times 10^{-3}$, this hysteresis should have a width of only about 1 mK in a perfectly homogeneous system in the absence of fluctuations and would not have been detected in the experiment. Figure 6 shows the Fourier transform power corresponding to this case; one sees that the power still increases continuously and gradually from the fluctuation values as $\Delta T_{c,exp}$ is exceeded. The images and the power yield $\Delta T_{c,exp} = 0.437 \pm 0.001$ K (see table 3), which deviates from the theoretical one in table 3 by 2 %.

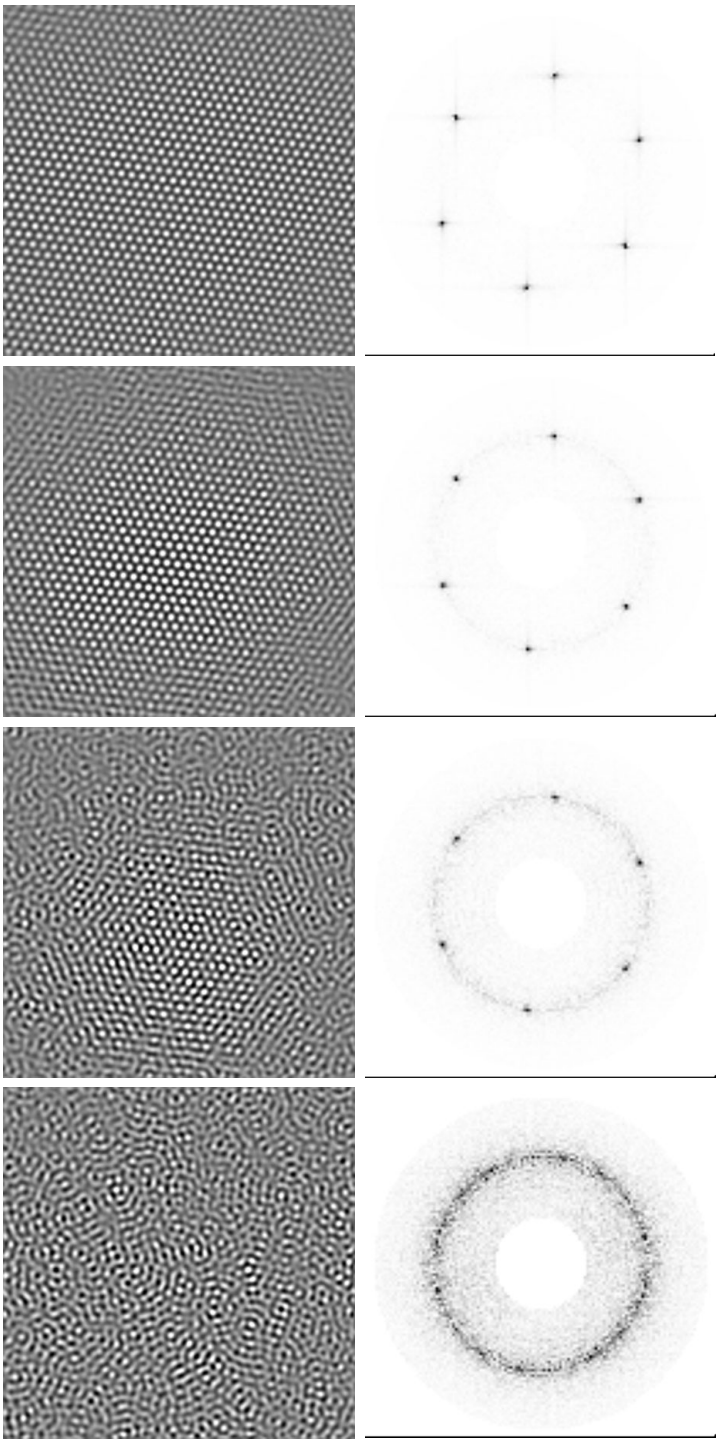

FIGURE 5. Shadowgraph images (left column) and the moduli of their Fourier transforms (right column) for (from bottom to top) $\Delta T = 0.4362$, 0.4368, 0.4375 and 0.4388 K at $P_{is} = 39.59$ bars and $T_m = 48.10\,^{\circ}\mathrm{C}$ (E-IV). Each image covers an area of 1.92×1.92 mm^2. The centre of the Fourier transform was removed to eliminate an instrumental noise peak near the origin. From these images we estimate $\Delta T_{c,exp} = 0.437 \pm 0.001$ K.

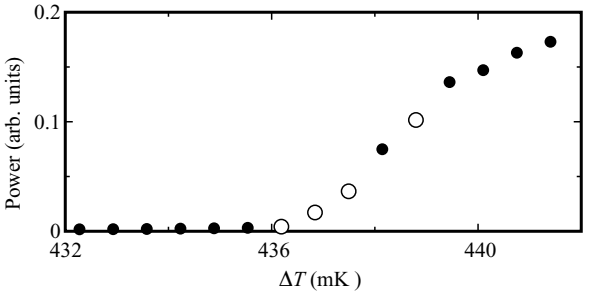

FIGURE 6. The total shadowgraph power as a function of ΔT for $P_{is} = 39.59$ bars and $T_m = 48.10\,^{\circ}\mathrm{C}$ (E-IV). The open circles correspond to the images shown in figure 5.

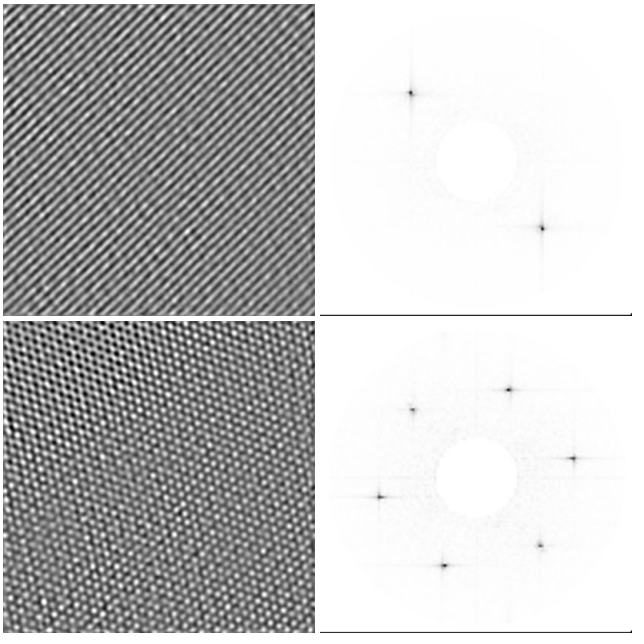

FIGURE 7. Shadowgraph images (left column) and the moduli of their Fourier transforms (right column) for (from bottom to top) $\Delta T = 0.5607$ and 0.5672 K at $P_{is} = 39.59$ bars and $T_m = 48.10\,^{\circ}\mathrm{C}$ (E-IV). Each image covers an area of 1.92×1.92 mm^2. The centre of the Fourier transform was removed to eliminate an instrumental noise peak near the origin. From these images we estimate $\Delta T_{hr} = 0.564 \pm 0.003$ K, corresponding to $\epsilon_{hr} = 0.29 \pm 0.01$.

As can be seen in figure 7, the hexagons persisted up to $\Delta T_{h,r} = 0.564 \pm 0.003$ K, where a transition to rolls occurred. This yields $\epsilon_{h,r} \equiv \Delta T_{h,r}/\Delta T_{c,exp} - 1 = 0.29 \pm 0.01$ for the hexagon to roll transition. Measurements were also made, by the same method, of the transition from rolls to hexagons that occurs as ΔT is reduced from high values. They yielded $\epsilon_{r,h} = 0.26 \pm 0.01$, somewhat lower than the experimental value of $\epsilon_{h,r}$. The quantitative agreement with the theory (see tables 4 or 8) is not really satisfactory. The transition point $\epsilon_{h,r}$ is comparable with $\epsilon_r \simeq 0.3$ where according to the amplitude-equation description stable rolls exist. However, $\epsilon_{h.r}$ is considerably below the theoretical estimate $\epsilon_{T'} = 0.42$ for the point where the potentials of the hexagons and rolls become equal. Apart from uncertainties with respect to the

material parameters, the discrepancies might be attributed to a problematic use of the weakly nonlinear analysis at larger ϵ, as has been discussed in § 4.1.

A more extreme case of classical NOB convection was found by increasing T_m further on the same isobar to $T_m = 48.30\,^{\circ}\mathrm{C}$ (E-V). In that case the classical estimate yields, according to table 4, a very large $Q = 15$ and $\epsilon_a = -0.038$. Thus one expects a well-resolved hysteresis loop. Its existence is indeed clearly confirmed by the experimental images in figure 8 (each of these images was taken after equilibration at a given ΔT for 40 min; only every second step of ΔT is shown) and the corresponding Fourier power shown in figure 9.

From these data we estimate $\Delta T_{c,exp} = 0.6728 \pm 0.0006$ K which implies a reduction compared to $\Delta T_{c,OB}$ by a factor of 0.79. Inspection of table 3 shows that the reduction of $\Delta T_{c,OB}$ is also predicted by the theory, but by a smaller amount corresponding to a factor of 0.89. The experimental width of the hysteresis loop ΔT_s is about -3.3 ± 0.6 mK, yielding $\epsilon_s = \Delta T_s / \Delta T_c = -0.005 \pm 0.001$. This value is considerably smaller than the theoretical value based on the full numerical calculation $\epsilon_a = -0.011$ (see table 8), while the classical NOB approach would predict an even larger $\epsilon_a = -0.038$ (see table 4). Part of this discrepancy may be due to a fluctuation-induced transition to hexagons at a slightly negative ϵ, and to a transition from hexagons to fluctuations at ϵ_T rather than at ϵ_a. However, we attribute the majority of the discrepancy to an inadequately accurate knowledge of the material parameters. In contrast to E-IV, a transition from hexagons to rolls is not observed for the run E-V within the range of our experiment. This is consistent with the large theoretical values of ϵ_r and ϵ_b in tables 4 and 8, which are, however, not reliable from a quantitative point of view (see the discussion in § 4.1).

4.4. *Non-Boussinesq effects on the critical isochore*

Finally, we consider the cases on the lower two solid curves in figure 1. For these $\rho(T_m)$ is equal or very close to ρ^* and the odd-in-$\tilde{\delta}$ terms of the fluid properties should be very small as already discussed in § 2. One finds that Q is quite small as well (see table 4), consistent with the numerical values of the stability limits in table 8. Thus we do not expect classical NOB effects for these cases. Images for the case of $P_{is} = 38.09$ bars at $T_m = 46.22\,^{\circ}\mathrm{C}$ are shown in figure 10. They reveal a transition from fluctuations to rolls, with no evidence of hexagonal structures. We obtained $\Delta T_{c,exp} = 0.131$ K, which is larger by a factor 1.21 than the OB value 0.108 K, in modest agreement with the theory (see table 3).

From table 4 one sees that the case $P_{is} = 38.33$ bars (E-II) has a Q-value that is even smaller than that of the $P_{is} = 38.09$ bars case. Thus, at the level of classical theory and also in line with the stability limits shown in table 8, the classical NOB effects should be even smaller, although they would be expected to be unnoticeable in either case. A transition from fluctuations to rolls indeed is found without any hint of hexagons, but $\Delta T_{c,exp} = 0.440$ K is larger than the OB value $\Delta T_{c,OB} = 0.235$ K by a factor of 1.86 compared to the corresponding ratio 1.2 for E-I discussed before. The agreement with the theoretical ratio 1.82 in table 3 is very good.

4.5. *Summary of experimental results*

We demonstrated that the experiments on the critical isochore (E-I, E-II, E-III) agree quite well with the theoretical calculations. They are characterized by a fairly small Busse parameter Q; thus only rolls should be observable at onset as is indeed the case. The measurements show a significant shift of $\Delta T_{c.exp}$ relative to the Boussinesq value, in good overall agreement with the theory presented in § 5.2.

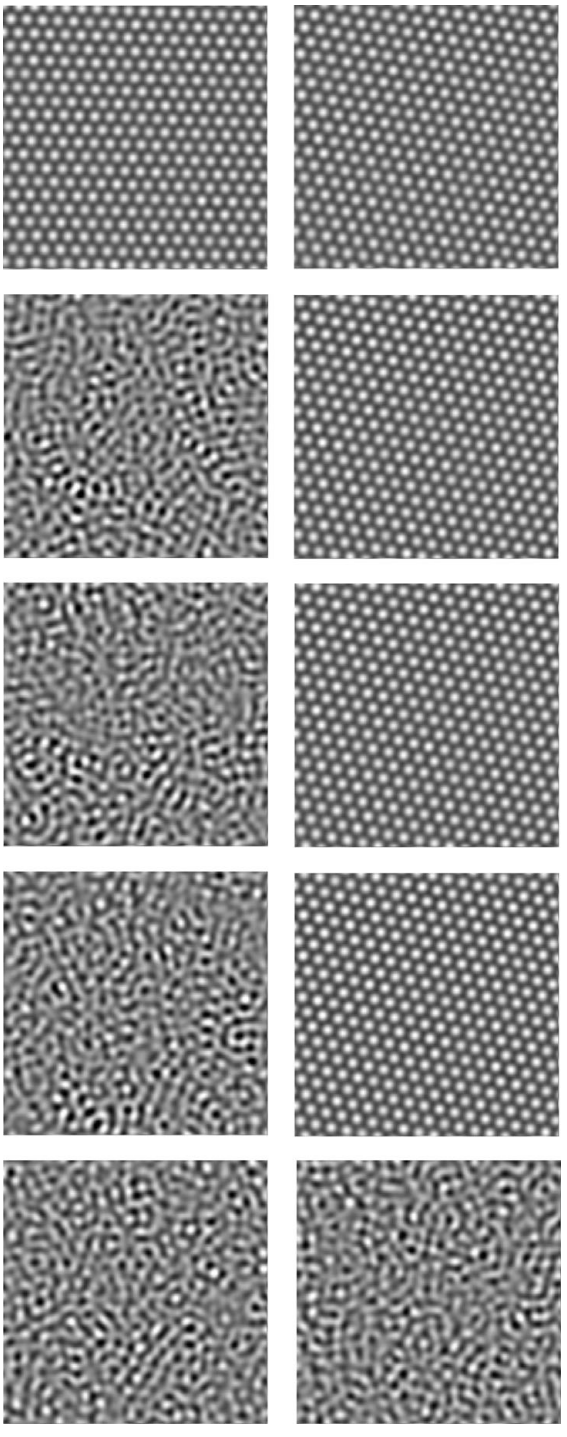

FIGURE 8. Shadowgraph images of size 0.96×0.96 mm^2 (each image has its own grey scale, chosen on the basis of the variance of the image). From bottom to top, the images are for $\Delta T = 0.6685$, 0.6698, 0.6712, 0.6725 K and 0.6738 K at $P_{is} = 39.59$ bars and $T_m = 48.30\,^{\circ}$C (E-V). The left column was taken with increasing ΔT, and the right column with decreasing ΔT. The hysteresis associated with the transcritical bifurcation is apparent.

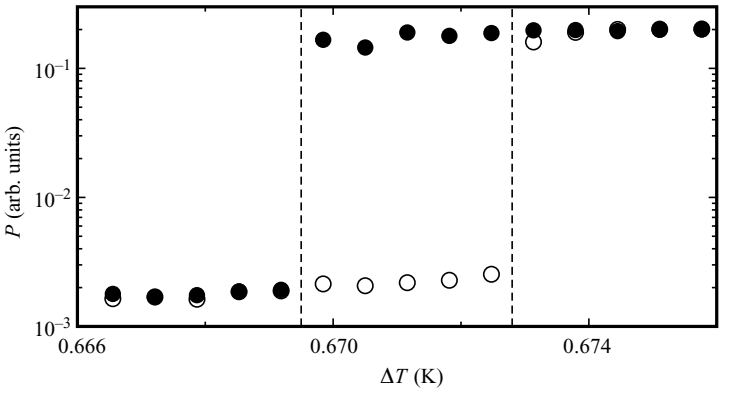

FIGURE 9. The shadowgraph intensity (in arbitrary units) on a logarithmic scale as a function of the temperature difference ΔT on a linear scale at $P_{is} = 39.59$ bars and $T_m = 48.30\,^{\circ}$C (E-V). Open circles: increasing ΔT; solid circles: decreasing ΔT. The vertical dashed lines correspond to the best experimental estimates of the transitions.

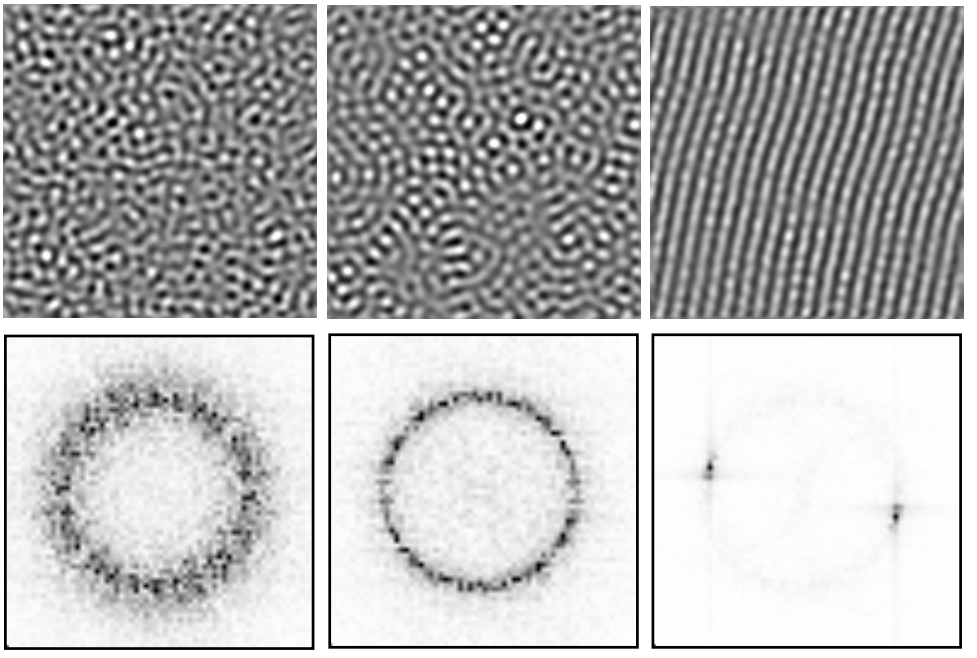

FIGURE 10. Shadowgraph images of size 1.28×1.28 mm^2 and the moduli of their Fourier transforms for $P_{is} = 38.09$ bars and $T_m = 46.22\,^{\circ}$C (E-I). From left to right, the images are for $\Delta T = 0.125$ K, 0.131 K and 0.132 K.

In the experiment E-IV with a moderate $Q = 4.66$, slightly away from the critical isochore, one observes the classical NOB scenario: a bifurcation to hexagons at onset followed by a transition to rolls at higher ϵ. Consistent with theoretical expectations, the hysteresis at onset was too small to be observable in this case. The transition to rolls occurred at a value of $\epsilon_{h,r} \simeq 0.29$, close to the point $\epsilon_r = 0.30$ where rolls are predicted to first become stable, but well below the point $\epsilon_{T'} = 0.41$ (see table 4 and §4.3) where rolls acquire a lower potential than hexagons. For completeness

we mention another system with $Q \simeq 4$, namely CO_2 away from the critical point (Bodenschatz *et al.* 1991; see also § 6.1). In that case the small hysteresis at onset could be resolved because the temperature differences involved were two orders of magnitude larger than those of the present work. Here theory and experiment agree very well, but in contrast to the present case the linear approximation to the material properties (2.7) is quite accurate. The largest quantitative discrepancies between theory and experiment are found in the case of E-V, where only hexagons are observed near onset (for details, see § 4.3). In this case the hysteresis at onset was resolved very well, but found to be smaller by about a factor of 2 than the theoretical value. Since the distance to the critical isochore is larger than for E-IV, the material parameters are less well known in this case. In addition, as discussed in § 4.1, the weakly nonlinear analysis becomes questionable due to the very large Busse parameter $Q = 15$.

5. Theory of non-Boussinesq effects and the linear regime

In this section we first lay the general foundations of our theoretical treatment of NOB effects in terms of an appropriate hydrodynamic description. The analysis is simplified considerably by using an analytic description of the material parameters as functions of temperature in terms of Padé approximants. Within a linear stability analysis of the heat-conducting basic state of the fluid layer we then determine the critical temperature difference ΔT_c. It can differ substantially from the OB value $\Delta T_{c,OB}$, as anticipated already in table 3. A weakly nonlinear treatment of NOB effects is deferred to the next section.

5.1. *On the temperature and pressure dependence of the material properties*

In figure 2 we already showed a representative example of the heat capacity C_p as a function of the dimensionless temperature $\tilde{\delta} = (T - T_m)/\Delta T_{c,OB}$ on the isobar of the experimental run E-I; further relevant material parameters are shown in figure 11. It turns out that their temperature dependences can be described very well in closed form by rational functions of $\tilde{\delta}$ in the form of Padé approximants. To achieve an accuracy of better than 0.05 % it is sufficient to restrict the degrees of the polynomials in the numerator and the denominator of the Padé approximant to be less than 5.

For instance, $\hat{\rho}(\tilde{\delta}) \equiv \rho(\tilde{\delta})/\rho_m$ can be represented by

$$\hat{\rho}(\tilde{\delta}) = \frac{1 + \rho_1\tilde{\delta} + \rho_2\tilde{\delta}^2 + \rho_3\tilde{\delta}^3 + \rho_4\tilde{\delta}^4}{1 + \rho_5\tilde{\delta}^2 + \rho_6\tilde{\delta}^4}, \tag{5.1}$$

where ρ_m denotes the density at $T = T_m$, i.e. at $\tilde{\delta} = 0$. Thus the reduced thermal expansion coefficient $\alpha(T)/\alpha(T_m) = -\rho(T)^{-1}\partial_T\rho(T)/\alpha(T_m)$ as function of $\tilde{\delta}$ is given by

$$\hat{\alpha}(\tilde{\delta}) \equiv \frac{\alpha(\tilde{\delta})}{\alpha_m} = -\frac{\partial_{\tilde{\delta}}\hat{\rho}(\tilde{\delta})}{\rho_1}\hat{\rho}(\tilde{\delta})^{-1}$$
$$\text{with} \quad \alpha_m \equiv \alpha(0) = -\rho_1/\Delta T_{c,OB}. \tag{5.2}$$

In analogy to $\hat{\rho}(\tilde{\delta})$ in (5.1), we fit all fluid properties, i.e. the set $X = (\hat{\rho}, \hat{\alpha}, \hat{C}_p, \hat{\eta}, \hat{\lambda})$, normalized by their values at $\tilde{\delta} = 0$ (i.e at $T = T_m$), by a Padé approximant

$$X = \frac{1 + x_1\tilde{\delta} + x_2\tilde{\delta}^2 + x_3\tilde{\delta}^3 + x_4\tilde{\delta}^4}{1 + x_5\tilde{\delta}^2 + x_6\tilde{\delta}^4}. \tag{5.3}$$

Note that in general we kept only even powers of $\tilde{\delta}$ in the denominators in order to be able to separate more easily the parts that are even and odd in $\tilde{\delta}$. In table 5 we listed

	$\hat{\rho}$	$\hat{\alpha}$	$\hat{C}_p$	$\hat{\eta}$	$\hat{\lambda}$
x_1	−0.266	0.170	0.230	−0.336	−0.035
x_2	4.961	3.133	3.130	5.710	26.080
x_3	−0.837	0.292	0.260	−1.260	−2.110
x_4	1.503	0	0	1.950	79.350
x_5	4.93	8.53	8.44	5.63	26.71
x_6	1.49	5.73	5.30	1.95	91.93

TABLE 5. Padé coefficients x_i (5.3) for the members of the material-parameter set X for the experimental run E-I

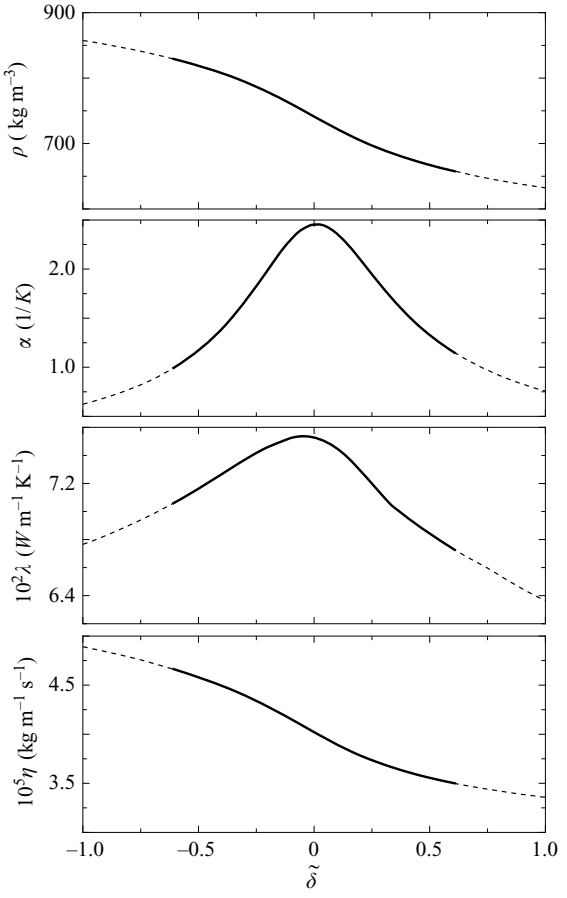

FIGURE 11. The fluid properties along the isobar $P_{is} = 38.09$ bars (E-I) as a function of $\tilde{\delta} = (T - T_m)/\Delta T_{c,OB}$. Dotted lines: Data taken from the literature as detailed in § 2. Heavy solid lines: Padé approximants, (5.3), to the material properties with the coefficients listed in table 5 over the temperature range covered at the experimental onset of convection.

the Padé coefficients for the representative experimental run E-I. The corresponding Padé approximants for the material properties have been included in figure 11; they fit the data extremely well.

While the temperature dependences of the material properties play an important role, we shall now demonstrate by some rough estimates that the variations of these properties with pressure are unimportant for the present experiments. Because of the divergence of the isothermal compressibility k_T (2.4) at T^*, the density is very sensitive to pressure variations. To get a feeling for the relevance of k_T in our case we consider the experiment E-I where T_m is closest to T^*. In the conduction state the hydrostatic pressure is determined by

$$\frac{\mathrm{d}p}{\mathrm{d}z} + g\rho = 0. \tag{5.4}$$

Thus the hydrostatic pressure difference Δp between the lower and the upper plate is of the order of $gd\rho_m \simeq 2.5 \times 10^{-6}$ bars which is very small compared to the average pressure $P_{is} \simeq 40$ bars. The pressure drop Δp is associated with a difference $\Delta\rho > 0$ of the density between the lower and the upper plate. Using the data for $k_{T,m}$ and ρ_m from table 2 one finds $\Delta\rho \simeq k_{T,m}\rho_m \Delta p \simeq 1.5 \times 10^{-4}\rho_m$. This pressure-induced variation of ρ is negligible compared to that introduced by the critical temperature difference ΔT_c which is of the order of $\rho_m \alpha_m \Delta T_c \sim 0.25\rho_m$.

While ρ determines the buoyancy force in the momentum balance, the energy balance (see e.g. Landau & Lifshitz 1987) requires the analysis of the temperature and pressure dependences of the entropy $S(T, p)$. With the use of

$$TdS = C_p dT + T\rho^{-1}\alpha dp, \tag{5.5}$$

the estimate $C_{p,m}\Delta T_c \approx 10^4$ J kg^{-1} of the first term on the r.h.s. of (5.5) is much larger than the estimate $T\rho^{-1}\alpha\Delta p \approx 2$ J kg^{-1} of the second one. Moving away with T_m from T^* (E-II $\rightarrow$ E-V), the relative importance of the pressure dependence is further reduced. Thus in the case of a small cell thickness d and not in the immediate vicinity of T^* as in the present experiments the pressure dependence of ρ and *a fortiori* of the other material parameters can be safely neglected.

5.2. *Basic equations and linear properties*

We deal with a viscous fluid layer of thickness d and large lateral dimension L, i.e. of large aspect ratio $\Gamma = L/d \gg 1$. We use a Cartesian coordinate system with the horizontal directions x, y perpendicular to gravity $\boldsymbol{g}$ which in turn is antiparallel to the z direction, i.e. $\boldsymbol{g} = g(0, 0, -1)$. The position vector $\boldsymbol{r}$ will appear in the following notations: $\boldsymbol{r} \equiv (x, y, z) \equiv (\boldsymbol{x}, z) \equiv (x_1, x_2, x_3)$.

The fluid velocity $\boldsymbol{u} = (u_1, u_2, u_3)$ is determined by the Navier–Stokes equation, supplemented by the bulk force from gravity:

$$\partial_t(\rho u_i) + \partial_j(\rho u_j u_i) = -\partial_i p - \rho g \delta_{i3} + \partial_j \boldsymbol{\tau}_{i,j} \tag{5.6}$$

with the pressure p and the stress tensor

$$\boldsymbol{\tau}_{i,j} = \eta(\partial_i u_j + \partial_j u_i) + \eta_v \delta_{i,j} \partial_k u_k, \tag{5.7}$$

where δ_{ij} denotes the Kronecker delta and η_v the bulk viscosity. We assume the Einstein summation convention throughout the paper.

Mass conservation leads to the continuity equation

$$\partial_t \rho + \partial_j(\rho u_j) = 0. \tag{5.8}$$

Starting from the entropy balance and neglecting the pressure dependence as discussed before we obtain finally the governing equation for the temperature T (see e.g. Landau

& Lifshitz 1987):

$$\partial_t T + u_j \partial_j T = \frac{1}{\rho C_p} \partial_j (\lambda \partial_j T). \tag{5.9}$$

As usual we have omitted viscous heating. The coupled system of the partial differential equations (PDE) (5.6), (5.8), (5.9) has to be solved after implementing the explicit Padé approximants (5.3) for the material properties as functions of the temperature T. We are mainly interested in the stationary solutions of the PDEs, where the momentum density $\boldsymbol{v} = \rho \boldsymbol{u}$ is a solenoidal field (see (5.8)). Thus $\boldsymbol{v}$ can be represented in the standard poloidal–toroidal decomposition by two velocity potentials f, ψ:

$$\begin{aligned} &\boldsymbol{v} = \boldsymbol{\delta} f + \boldsymbol{\zeta} \psi \quad \text{with} \\ &\boldsymbol{\delta} = \left(\partial_x \partial_z, \partial_y \partial_z, -\partial_x^2 - \partial_y^2\right), \quad \boldsymbol{\zeta} = (\partial_y, -\partial_x, 0). \end{aligned} \tag{5.10}$$

One big advantage of this representation is that one gets rid of the pressure p and the contribution of the volume viscosity η_v by operating on the velocity equation (5.6) with $\boldsymbol{\delta}$ and $\boldsymbol{\zeta}$ (5.10), respectively.

It is very common in the literature (anelastic approximation, see e.g. Gough 1969) to neglect the time derivative $\partial_t \rho$ in the continuity equation (5.8) not only for the steady state but also in the case of slow dynamics. This assumes for instance that velocities are much smaller than the sound velocity, i.e. that the Mach number is small. For our problem this is always the case. Thus, in line with Busse (1967), the introduction of velocity potentials remains possible and permits the elimination of the pressure.

In our analysis we adopt periodic boundary conditions in the plane, which are appropriate for large-aspect-ratio systems. Consequently, we can switch in explicit calculations from position space (x, y) to the two-dimensional Fourier space with wave vector $\boldsymbol{q} = (q, p)$. At the top and bottom plates we choose realistic no-slip boundary conditions for the velocity field $\boldsymbol{u}$ and keep the temperatures fixed:

$$\boldsymbol{u} = 0 \text{ at } z = \pm\frac{d}{2}, \tag{5.11}$$

$$T = T_m + \frac{\Delta T}{2} \text{ at } z = -\frac{d}{2},$$

$$T = T_m - \frac{\Delta T}{2} \text{ at } z = +\frac{d}{2}. \tag{5.12}$$

Here, as before, T_m denotes the mean temperature and $\Delta T > 0$ the temperature difference across the layer.

Let us first calculate the basic state solution $T = T_{cond}(z)$ where $\boldsymbol{u} = 0$. According to (5.9), one has to solve the equation

$$\begin{aligned} &\hat{\lambda}(\delta_0) \frac{\mathrm{d}\delta_0(z)}{\mathrm{d}z} \mathrm{d}z = C_1 \text{ with} \\ &\delta_0(z) = \frac{T_{cond}(z) - T_m}{\Delta T_{c,OB}}. \end{aligned} \tag{5.13}$$

The constant C_1 has to be adjusted to guarantee the boundary condition

$$\delta_0(z = \pm d/2) = \pm\frac{1}{2}\frac{\Delta T}{\Delta T_{c,OB}} = \pm\frac{1}{2}\frac{R}{R_{c,OB}}, \tag{5.14}$$

where we have used again the definition $R = \Delta T / T_s$ (2.1) and consequently $R_{c,OB} = \Delta T_{c,OB} / T_s$.

With the use of the Padé approximant for $\hat{\lambda}\delta(z_0)$ in (5.13) one obtains $z(\epsilon_0)$ analytically by direct integration. The inversion of $z(\delta_0)$ leading to $\delta_0(z)$ is done numerically. For the present experiments the temperature dependence of $\hat{\lambda}$ is rather weak and $T_{cond}(z)$ may be represented to an accuracy of better 0.01 % by

$$\begin{aligned} T_{cond}(z)/T_s &= T_m/T_s + RZ(z), \\ Z(z) &= -z/d + w(z), \\ w(z) &= (z/d)^2 - 1/4)\left[t_0 + t_1(z/d) + t_2(z/d)^2\right]. \end{aligned} \tag{5.15}$$

After insertion of T_{cond} into (5.13) we arrive at

$$\delta_0(z) = \frac{RZ(z)}{R_{c,OB}}, \tag{5.16}$$

where obviously the boundary conditions (5.14) are fulfilled. The coefficients t_i are small: for the experiment E-I we obtain, for instance, $t_0 = -0.026$, $t_1 = 0.108$, $t_2 = 4.7\ 10^{-3}$. Thus the temperature T_m corresponds to the midplane of the cell ($z = 0$) up to an error of less than 1 %.

In the presence of convection T_{cond} (5.16) is modified by a convective temperature contribution $\Theta(\mathbf{x}, z) = T_s \theta(\mathbf{x}, z)$. Thus in general we have to replace the temperature variable $\tilde{\delta}$ in the Padé approximants (5.3) for the material parameters by

$$\tilde{\delta}(\mathbf{x}, z) = \frac{T - T_m}{\Delta T_{c,OB}} = \delta_0(z) + \theta(\mathbf{x}, z)/R_{c,OB}. \tag{5.17}$$

We are interested in the onset of convection and in the weakly nonlinear regime, where we keep as usual the field amplitudes up to cubic order. Since in this approximation the poloidal velocity potential ψ does not contribute, only θ and f have to be considered. Thus we have to expand the material parameters collected in X (see (5.3)) up to second order in θ except for the density ρ where we need the cubic contribution as well in the buoyancy term. For instance, the result for the reduced density $\hat{\rho}(\tilde{\delta}) = \rho(\tilde{\delta})/\rho_m$, keeping the leading terms, becomes

$$\hat{\rho}[\tilde{\delta}(\boldsymbol{x}, z)] = \rho^0(z) + \theta(\boldsymbol{x}, z)\rho^1(z) + \theta^2\rho^2(z) + \theta^3\rho^3(z) \tag{5.18}$$

with

$$\rho^0(z) = \hat{\rho}[\delta_0(z)], \quad \rho^n(z) = \frac{1}{n!}\frac{\partial^n \hat{\rho}\,[\delta_0(z)]}{\partial \delta_0^n}\frac{1}{[R_{c,OB}]^n} \quad \text{for } n > 0. \tag{5.19}$$

Analogous expansions with respect to θ are used for the other members of X (see (5.3)) which yield the expansion coefficients $\alpha^i(z), \eta^i(z), \ldots$, $i = 0, 1, 2$. With the use of (5.2), (2.2) the coefficients $\alpha^0(z)$ and $\rho^1(z)$ are related by

$$\rho^1(z) = -\alpha_m T_s \rho^0(z)\alpha^0(z). \tag{5.20}$$

To render the hydrodynamic equations dimensionless we use the usual scales for the length (d), time (d^2/κ_m), velocity (κ_m/d), pressure ($\nu_m \kappa_m \rho_m / d^2$) and temperature ($T_s$). Then the non-dimensionalized members of the material parameter set X (see (5.3)) come into play, which are expanded in terms of θ as indicated before.

It is convenient to introduce a symbolic notation of the hydrodynamic equations (5.6) and (5.9), the 'non-Boussinesq equations' (NBE), as used in this paper:

$$\partial_t \widehat{\mathscr{B}}(\partial_{\boldsymbol{x}}, \partial_z, z)\hat{\boldsymbol{V}}(\boldsymbol{x}, z, t) = \widehat{\mathscr{L}}(\partial_{\boldsymbol{x}}, \partial_z, z; R)\hat{\boldsymbol{V}}(\boldsymbol{x}, z, t) + \boldsymbol{N}, \tag{5.21}$$

with the symbolic vector $\hat{\boldsymbol{V}}(\boldsymbol{x}, z, t) = (f, \theta)$. The nonlinearity $\boldsymbol{N}$ contains the components of $\hat{\boldsymbol{V}}$ and their spatial derivatives up to cubic order. The following boundary conditions for θ, f have to be satisfied:

$$\theta(\boldsymbol{x}, \pm 1/2) = f(\boldsymbol{x}, \pm 1/2) = \partial_z f(\boldsymbol{x}, \pm 1/2) = 0. \tag{5.22}$$

They follow from (5.11), (5.12).

For our purpose it is not illuminating to show the bulky expressions for the nonlinearity $\boldsymbol{N}$ (5.21), which are handled by using Mathematica. For definiteness, however, we show explicitly the linear operators $\widehat{\mathscr{B}}, \widehat{\mathscr{L}}$ which determine the linear part of (5.21):

$$\begin{aligned} \frac{1}{\sigma}\partial_t \nabla^2 \Delta_2 f &= -\alpha^0(z)\rho^0(z)\Delta_2\theta + \delta_i \partial_j \boldsymbol{\tau}_{i,j}, \\ \rho^0(z) C_p^0(z)\partial_t\theta &= RC_p^0(z) v_z \partial_z Z(z) + \partial_j(\lambda^0(z)\partial_j\theta) + R\partial_z\left[\lambda^1(z)\theta\partial_z Z(z)\right] \end{aligned} \tag{5.23}$$

with the Prandtl number $\sigma = \nu_0/\kappa_0$ and the two-dimensional Laplacian $\Delta_2 = \partial_x^2 + \partial_y^2$. The linearized stress tensor is $\boldsymbol{\tau}_{i,j}$ given as

$$\boldsymbol{\tau}_{i,j} = \eta^0(z)\left[\partial_i(v_j/\rho^0(z)) + \partial_j(v_i/\rho^0(z))\right]. \tag{5.24}$$

The contribution $\propto \rho^0(z)$ of the buoyancy term has been combined with the pressure, which is then eliminated by exploiting $\delta_i\partial_i = 0$. Note that the main control parameter R appears not only explicitly in (5.23) but also implicitly via $\delta_0(z)$ (see (5.16)) in the material parameters. It is obvious that one will return to the OB equations by neglecting the z dependence of the material parameters by choosing $\rho^0, \alpha^0, \eta^0, C_p^0, \lambda^0 = 1$ and $\lambda^1 = 0$. In the NOB analysis of Busse, only the corrections linear in z of the material parameters are kept.

Switching to Fourier space in (5.23) by the ansatz $\hat{\boldsymbol{V}} = \mathrm{e}^{\Lambda t}\mathrm{e}^{\mathrm{i}\boldsymbol{q}\cdot\boldsymbol{x}}\boldsymbol{U}(\boldsymbol{q}, z)$ leads to the eigenvalue problem

$$\Lambda\mathscr{B}(\boldsymbol{q}, \partial_z, z)\boldsymbol{U}(\boldsymbol{q}, z) = \mathscr{L}(\boldsymbol{q}, \partial_z, z; R)\boldsymbol{U}(\boldsymbol{q}, z), \tag{5.25}$$

where the operators $\mathscr{B}, \mathscr{L}$ derive from $\widehat{\mathscr{B}}, \widehat{\mathscr{L}}$, respectively by substituting $\partial_{\boldsymbol{x}} \to \mathrm{i}\boldsymbol{q}$.

The discrete set of the eigenvalues of $\Lambda_i(\boldsymbol{q}, R), i = 0, 1, 2, \ldots$ of the eigenvalue problem (5.25) are assumed to be ordered in decreasing order with respect to their real parts: $\Re\Lambda_0 \geqslant \Re\Lambda_1 \geqslant \Re\Lambda_2 \ldots$. When for increasing R the growth rate $\Re\Lambda_0(\boldsymbol{q}, R)$ crosses zero at $R_0(\boldsymbol{q})$ (neutral surface) and becomes positive, the homogeneous basic state becomes unstable to convection. The minimum of $R_0(\boldsymbol{q})$ defines the critical wave vector $\boldsymbol{q}_c$ and the threshold $R_c = R_0(\boldsymbol{q}_c)$. In the present case the bifurcation is stationary, since $\Im\Lambda_0(\boldsymbol{q}_c, R_c) = 0$. Furthermore, because of the isotropy of the present RBC system the eigenvalues Λ_i and the corresponding eigenvectors $\boldsymbol{U}_i$ depend only on $|\boldsymbol{q}|$.

To solve the eigenvalue problem (5.25) we use the standard Galerkin approach to guarantee the boundary conditions (5.22). Thus we expand θ, f with respect to the z dependence in terms of $S_n(z) = \sqrt{2}\sin[n\pi(z + 1/2)]$ and the Chandrasekar functions $C_n(z), n = 1, 2, \ldots, n_{cut}$, respectively, which are both normalized to 1. In this way (5.25) is mapped to a finite-dimensional algebraic eigenvalue problem, from which we obtain numerically via $\Lambda_0(\boldsymbol{q}, R)$ the critical Rayleigh number R_c and the critical wavenumber q_c. By monitoring the effect of increasing the cutoff n_{cut} we found that the choice $n_{cut} = 8$ is sufficient to obtain an accuracy of 0.1 % for R_c, q_c. All calculations in this paper were performed with the use of Mathematica.

In table 3 we already presented the resulting theoretical critical temperature differences $\Delta T_c = R_c T_s$ normalized by $\Delta T_{c,OB}$. For comparison we included $\Delta T_{c,exp}$ as well in that table. As already discussed in § 4, the theoretical ΔT_c match the $\Delta T_{c,exp}$ surprisingly well considering some uncertainties in the experimental data and in the precise knowledge of the material parameters. These uncertainties are presumably more pronounced for the runs E-I and E-V, where we find, in contrast to the very good agreement for E-II, E-III, E-IV, a difference of about 8 % for E-I and 10 % for E-V.

Now we are in the position to put our conjecture in § 2 to capture the NOB effects responsible for the differences between $\Delta T_{c,OB}$ and ΔT_c on a sound basis. There we proposed to replace α_m and $C_{p,m}$ by their averages $\overline{C}_p$ and $\overline{\alpha}$. If we solve the linear eigenvalue problem (5.25) which determines R_c in the so called one-mode approximation by truncating the Galerkin expansion at the leading term $n = 1$, we obtain in the OB limit $q_c = 3.098$, $R_c = 1728.4$ which deviates from the actual value $R_c = 1707.8$ by only 1 %. Inspection of (5.23) shows that in the one-mode approximation we return to the OB problem except that $\alpha^0(z)$, $C^0(z)$, $\lambda^0(z)$ are replaced, more precisely than speculated in § 2, by the weighted averages

$$\begin{aligned}\langle\alpha\rangle &= \int_{-1/2}^{1/2} \mathrm{d}z S_1(z)\alpha^0(z)C_1(z),\\ \langle C_p\rangle &= \int_{-1/2}^{1/2} \mathrm{d}z S_1(z)C_p^0(z)C_1(z),\\ \langle\lambda\rangle &= \int_{-1/2}^{1/2} \mathrm{d}z C_1(z)\lambda^0(z)C_1(z).\end{aligned} \tag{5.26}$$

The other functions $\rho^0(z)$ and $\eta^0(z)$, which are odd in z, are replaced by their OB values ($\rho^0(z) = \eta^0(z) = 1$). Thus, except that the control parameter R in (5.25) is replaced by

$$\tilde{R} = \frac{\langle\alpha\rangle\langle C_p\rangle}{\langle\lambda\rangle}\Delta T/T_s\ , \tag{5.27}$$

we have returned to the standard OB problem. Then $\tilde{R}_c = R_{c,OB}$ holds and we obtain the approximation

$$\Delta T_{c,app} = \frac{\langle\lambda\rangle}{\langle\alpha\rangle\langle C_p\rangle}\Delta T_{c,OB}, \tag{5.28}$$

for the critical temperature difference, consistent with the discussion in § 2. The ratios $\Delta T_{c,app}/\Delta T_{c,OB}$ for the five experimental runs already have been included in table 3, where they compare quite well with the exact $\Delta T_c/\Delta T_{c,OB}$.

6. Weakly nonlinear analysis of non-Boussinesq effects

The exploration of the fully nonlinear regime requires a demanding numerical treatment of the basic hydrodynamic equations discussed in § 5.2, which is outside the scope of this paper. In the vicinity of the onset ($\epsilon \approx 0$), however, the problem can be treated in the framework of the standard weakly nonlinear analysis to describe rolls and hexagons and their competition. The starting point is the following ansatz (see e.g. Ciliberto *et al.* 1988 and references therein) for the solutions $\hat{V}$ of the NBE (5.21)

in the cubic approximation:

$$\hat{\boldsymbol{V}}(\boldsymbol{x}, z, t) = \frac{1}{\sqrt{2}} \sum_{i=1}^{3} A_i(t) \mathrm{e}^{\mathrm{i}\boldsymbol{q}_i \cdot \boldsymbol{x}} \boldsymbol{U}_0(|\boldsymbol{q}_i|, z) + c.c, \tag{6.1}$$

where $\boldsymbol{U}_0(\boldsymbol{q}, z)$ is the eigenvector associated with the growth rate $\Lambda_0(\boldsymbol{q})$ of the eigenvalue problem (5.25). The wave vectors $\boldsymbol{q}_i$ present a resonant triad:

$$\boldsymbol{q}_1 + \boldsymbol{q}_2 + \boldsymbol{q}_3 = 0; \quad |\boldsymbol{q}_i| = q_c. \tag{6.2}$$

Following the standard convention, $\boldsymbol{U}_0(\boldsymbol{q}_i, z)$, which is non-zero for $-1/2 \leqslant z \leqslant 1/2$, is chosen to be real and positive.

Expanding (5.21) up to cubic order in the amplitudes A_i (for some details, see Appendix B) one arrives at the following well-known ODE for the amplitude A_1:

$$\tau_0 \partial_t A_1 = \epsilon A_1 - a A_2^* A_3^* - b A_1 \left(|A_2|^2 + |A_3|^2\right) - c A_1 |A_1|^2 \tag{6.3}$$

with the correlation time τ_0. The equations for A_2, A_3 are obtained by cyclic permutations of the indices 1, 2, 3. The coefficients a, b, c are real with $b, c > 0$ and $b > c$ in our case. It is well known that the stationary solutions of (6.3) can be chosen to be real as well. Besides the trivial (ϵ-independent) solution $A_i = 0$, which corresponds to the heat conduction state, we have first roll solutions $A_1 = A_r$, $A_2 = A_3 = 0$ with $A_r = \sqrt{\epsilon/c}$ if $\epsilon > 0$, which are stable for $\epsilon \geqslant \epsilon_r$. Furthermore stable hexagons ($A_1 = A_2 = A_3 \equiv A_h$) with

$$A_h = -\frac{a}{2(2b + c)} - sgn(a) \left(\frac{a^2}{4(2b + c)^2} + \frac{\epsilon}{2b + c} \right)^{1/2} \tag{6.4}$$

exist in an interval $\epsilon_a \leqslant \epsilon \leqslant \epsilon_b$. The explicit expressions for $\epsilon_a, \epsilon_h, \epsilon_r$ as well as the coexistence points $\epsilon_T, \epsilon_{T'}$ defined in § 2 are given in Appendix A. Note, that inspection of (6.1), (6.4) shows that the case $a > 0$ is associated with $\theta < 0$, i.e cold downflow in the centre of the hexagon.

For clarity it should be mentioned, that the normalization of the eigenvector $\boldsymbol{U}_0$ is not standardized in the literature. A transformation $\boldsymbol{U}_0 \to \tilde{\mathbf{U}}_{\mathbf{0}} = c_u \boldsymbol{U}_0$ leads according to (6.1) to redefined amplitudes $\tilde{A}_i = (c_u)^{-1} A_i$. They fulfil again the amplitude equation (6.3) but with the redefined coefficients $\tilde{a} = c_u a$, $\tilde{b} = c_u^2 b$, $\tilde{c} = c_u^2 c$. Note that quantities ϵ_a, ϵ_h, etc. given in Appendix A are invariant under this transformation, as they must be. We follow the normalization convention of Ciliberto *et al.* (1988), according to which the non-dimensional convective heat flow $\mathcal{N}$ is given as

$$\mathcal{N} \equiv \frac{(Nu - 1)R}{R_c} = \sum_{i=1}^{3} |A_i|^2, \tag{6.5}$$

where Nu denotes the Nusselt number, the ratio between the total heat flow and the conduction heat flow.

The amplitudes A_i are directly accessible in convection experiments since near $\epsilon = 0$ the shadowgraph intensity $I(\boldsymbol{x})$ is proportional to the vertical average of $\theta(\boldsymbol{x}, z)$ (see Trainoff & Cannell 2002). Thus the Fourier coefficients of $I(\boldsymbol{x})$ must be proportional to the amplitudes A_i. In fact the understanding of NOB patterns and their instabilities near onset have been greatly enhanced by using the concepts of amplitude equations (see e.g. Ciliberto *et al.* 1988; Bodenschatz *et al.* 1991).

6.1. *Busse revisited*

To obtain quantitative insight into the weakly nonlinear regime the coefficients a, b, c in (6.3) have to be calculated. In the approach of Busse (1967) the scaling $\gamma_i, A_i \sim O(\epsilon^{1/2})$ was implicitly assumed. Consequently it is sufficient to expand NBE (5.21) up to second order in θ, f and to linear order in the γ_i. Thus (5.21) simplifies as follows:

$$\widehat{\mathscr{B}}\partial_t \hat{\boldsymbol{V}} = \left(\widehat{\mathscr{L}}^0 + \sum_{k=0}^{4} \gamma_k \widehat{\mathscr{L}}_k^{\gamma}\right) \hat{\boldsymbol{V}}$$
$$-\boldsymbol{N}^0(\hat{\boldsymbol{V}}, \hat{\boldsymbol{V}}) - \sum_{k=0}^{4} \gamma_k \boldsymbol{N}_k^{\gamma}(\hat{\boldsymbol{V}}, \hat{\boldsymbol{V}}). \tag{6.6}$$

Here we have split the various terms of (5.21) into their OB part (superscript 0) and the contributions linear in the γ_i (superscript γ). The explicit expressions are, for instance, given in Busse (1967) or in Madruga, Riecke & Pesch (2007). All terms in (6.6) can be classified with respect to their symmetry properties under reflections at the midplane ($z \to -z$). A symbolic vector $\hat{\boldsymbol{V}}$ has the parity $\mathfrak{p} = 1(-1)$ if it is even (odd) in z. The application of $\widehat{\mathscr{L}}^0$ to $\hat{\boldsymbol{V}}$ with parity $\mathfrak{p}$ conserves the parity, while the application of the operators $\widehat{\mathscr{L}}_k^{\gamma}$ reverses the parity. Similarly, the nonlinearities are also characterized by a definite symmetry against reflections at the midplane: The term $\boldsymbol{N}^0(\hat{\boldsymbol{V}}_1, \hat{\boldsymbol{V}}_2)$ evaluated for $\hat{\boldsymbol{V}}_1, \hat{\boldsymbol{V}}_2$ with parities p_1, p_2, respectively, has the parity $\mathfrak{p} = -p_1 p_2$, while the corresponding parity of the $\boldsymbol{N}_k^{\gamma}$ operators is given as $\mathfrak{p} = p_1 p_2$.

The coefficients a, b, c have been calculated following the general procedure presented in Appendix B, where the extensive use of Mathematica has been very helpful. Our calculational scheme is equivalent to the original approach of Busse (1967), who used, however, a more tedious double expansion in the amplitudes A_i and the coefficients γ_i. Exploiting the symmetry properties of $\widehat{\mathscr{L}}^0$, $\widehat{\mathscr{L}}_k^{\gamma}$ and $\boldsymbol{N}^0$, $\boldsymbol{N}_k^{\gamma}$, it is easy to see that the cubic coefficients b, c are given by their well-known OB values up to corrections $O(\gamma_i^2)$. They read as follows (see e.g. Busse 1967; Pampaloni *et al.* 1992):

$$c = 0.69946 - 0.00472/\sigma + 0.008325/\sigma^2,$$
$$b = 0.99069 + 0.07675/\sigma + 0.097645/\sigma^2. \tag{6.7}$$

In contrast the quadratic coefficient a, which vanishes in the OB case, is of order γ_i. It is determined by the Busse parameter Q as follows:

$$a = \frac{3}{R_{c,OB}} Q, \tag{6.8}$$

where Q according to (2.9) is determined by the material properties via the γ_i and the coefficients $\mathscr{P}_i$. In Busse (1967), the coefficients $\mathscr{P}_i$ have been calculated in the limit $\sigma \to \infty$ for rigid boundary conditions. They agree very well with our results in (2.10) except that $\mathscr{P}_3 = 2.9197$ as given by Busse is much smaller than our value $\mathscr{P}_3 = 9.54$. The discrepancy can be traced back to a book-keeping error in Busse (1967). The corrections $\propto 1/\sigma$ were only given for free boundary conditions by Busse and they have been assumed in the literature to be approximately equal to those for the rigid case. This is in fact not correct, since they differ by up to 100 %. Furthermore it can be proven rigorously both for rigid and free boundary conditions (F. Busse, private

$\delta_\epsilon(i,j)\times 10^2$	0	1	2	3	4
0	1.876				
1	−0.732	−0.760			
2	10.543	4.994	−5.159		
3	2.470	−13.396	1.494	6.697	
4	0.366	−3.037	2.250	6.699	−0.190

TABLE 6. Coefficients $\delta_\epsilon(i,j)$ determining the NOB corrections of R_c from (6.9); $0 \leqslant j \leqslant 4$ (column index) and $0 \leqslant i \leqslant j$ (row index).

$\delta_q(i,j)\times 10^3$	0	1	2	3	4
0	−4.711				
1	−0.945	3.337			
2	8.395	−5.472	−4.508		
3	3.351	−11.110	2.960	5.553	
4	0.473	7.374	−2.736	−5.545	0.834

TABLE 7. Coefficients $\delta_q(i,j)$ (arranged as in table 6) determining the NOB corrections of q_c from (6.9).

communication, 2008) that the correction term $\propto 1/\sigma$ in $\mathscr{P}_3$ vanishes identically. This is confirmed in (2.10), while in Busse the $1/\sigma$ correction to $\mathscr{P}_3$ is not vanishing.

The analysis presented so far is strictly valid only in the limit $\gamma_i \to 0$, but the resulting expressions are commonly used for finite γ_i as realized in the experiments. Thus we will briefly discuss the corrections at larger γ_i. Let us start with the γ_i dependence of the critical Rayleigh number R_c on the basis of (6.6). Since the $\widehat{\mathscr{L}}_k^\gamma$ have the opposite parity of $\widehat{\mathscr{L}}^0$, the leading corrections to the OB values $R_{c,OB} = 1707.8$ and $q_{c,OB} = 3.117$ are of the order $O(\gamma_i^2)$ and have the following general representations:

$$\begin{aligned} \frac{R_c - R_{c,OB}}{R_{c,OB}} &= \sum_{i=0}^{4}\sum_{j=0}^{i} \delta_\epsilon(i,j)\gamma_i\gamma_j, \\ \frac{q_c - q_{c,OB}}{q_{c,OB}} &= \sum_{i=0}^{4}\sum_{j=0}^{i} \delta_q(i,j)\gamma_i\gamma_j. \end{aligned} \tag{6.9}$$

The expansion coefficients $\delta_\epsilon(i,j), \delta_q(i,j)$ are available from (6.6) by solving the corresponding linear eigenvalue problem in the framework of a standard second-order approximation with respect to the γ_i. But to be consistent one has in addition to expand the linear operator $\widehat{\mathscr{L}}$ (5.21), (5.23) to second order in the γ_i. The resulting expression $\widehat{\mathscr{L}}^{\gamma\gamma}$, which is a bilinear form in the γ_i, is quite lengthy and will not be shown here. Since $\mathscr{L}^{\gamma\gamma}$ is of even parity, the corresponding corrections to $R_{c,OB}$ and $q_{c,OB}$, which can be represented as in (6.9), can be captured already by a first-order perturbation analysis with respect to $\widehat{\mathscr{L}}^{\gamma\gamma}$. In fact the resulting corrections compensate to a large extent the quadratic ones from $\mathscr{L}^\gamma$. The whole analysis can be performed quasi-analytically and requires only the evaluation of certain matrix elements with the help of Mathematica. The final coefficients are listed in the tables 6 and 7.

To give an impression of the order of magnitude of the NOB-corrections we consider as a representative example the experiment described by Bodenschatz *et al.*

(1991) (see also Bodenschatz *et al.* 2000, p. 744). Here CO_2 is used as fluid for a cell of thickness $d = 52.5$ μm, with a pressure of 23.2 bars and $T_m = 27.35\,^{\circ}\mathrm{C}$. We obtain $\sigma = 0.874$, $\gamma_0 = 0.1512$, $\gamma_1 = -0.2137$, $\gamma_2 = 0.2366$, $\gamma_3 = 0.0769$, $\gamma_4 = -0.0810$. Since $Q = 3.8$ the NOB corrections were large enough to resolve the stability limits ϵ_a, ϵ_r, etc. in the experiment.

The corrections to $R_{c,OB}$ and $q_{c,OB}$ are in fact very small. With $n_{cut} = 8$ we obtain the values $R_{c,OB} = 1707.8$, $q_{c,OB} = 3.117$ for $\gamma_i = 0$, compared to $R_c = 1708.89$, $q_c = 3.1195$ from (5.23) for the finite γ_i. The differences $\Delta R = R_c - R_{c,OB}$ and $\Delta q = q_c - q_{c,OB}$ are described by (6.9) and the coefficients in tables 6 and 7 to an accuracy of better than 0.01 %. Even if we would multiply, as an example, all γ_i by a factor of 5, the analytical correction formula describes the modifications of $R_{c,OB}, q_{c,OB}$ to an accuracy of about 2 %. Note that disregarding the contribution of $\mathscr{L}^{\gamma\gamma}$ to the coefficients in tables 6 and 7 would instead produce a discrepancy of more than 20 % in this case.

Let us now address the coefficients a, b, c in (6.3) at finite γ_i, which determine the various stability limits $\epsilon_a, \epsilon_b, \epsilon_r$, etc. as given in Appendix A . The coefficients can be obtained only numerically by performing a weakly nonlinear analysis on the full NBE (5.21) as described in § 6. As a test the γ_i for CO_2 given above have been reduced at first by a factor of 10. Then they should be small enough that the analytical expressions a, b, c (defined in (6.8), (6.7)) apply, where Q is given by (2.9). According to Appendix A we arrive thus at $\epsilon_a = -2.038 \times 10^{-5}$, $\epsilon_b = 2.6434 \times 10^{-3}$, $\epsilon_r = 7.12 \times 10^{-4}$, $\epsilon_T = 1.002 \times 10^{-3}$. In fact the corresponding numerical stability limits fit these values to an accuracy of better than 0.05 %. This excellent agreement serves also as a convincing test for the correctness of the coefficients $\mathscr{P}_i$ (2.10), which determine via (2.9), (6.8) the coefficient a.

If we return to the unmodified γ_i of CO_2, we obtain instead on the basis of (5.21) the stability limits $\epsilon_a = -2.14 \times 10^{-3}$, $\epsilon_b = 2.907 \times 10^{-1}$, $\epsilon_r = 7.87 \times 10^{-2}$, $\epsilon_T = 1.11 \times 10^{-3}$. These values agree with the corresponding analytical ones, where again the coefficients (6.8), (6.7) are used in Appendix A, up to an accuracy of about 10 %.

In conclusion, we have shown that for situations, where the material properties are well described by keeping only the linear corrections (2.7), the critical values q_c, R_c are practically identical with the OB values. Moreover, the nonlinear properties are also well described by the closed expressions for the stability boundaries in Appendix A with the use of explicit coefficients given in (6.7, 6.8).

6.2. *Strong NOB corrections*

In the case of strong NOB effects as in a fluid near its critical point we have already demonstrated in § 5.2 that considerable modifications of R_c take place. These cannot be obtained by restricting the analysis to the linear corrections of the material properties in terms of the γ_i as in § 6.1. In this section we study the weakly nonlinear aspects of SF_6 in the framework of amplitude equations (6.3), where the NOB effects are strong compared to the classical Busse approach in § 6.1. For that purpose we have determined the coefficients a, b, c fully numerically from (5.21) by using the procedure described in Appendix B. For the material properties we use the Padé approximants discussed in § 5.1.

It is obvious, that the strong NOB effects do not only modify the coefficient a (defined in (6.8)) given in the previous section, but lead also to changes of the other coefficients b, c (defined in (6.7)), which all determine the stability limits according to Appendix A. We have not disentangled the various contributions to the stability limits listed in table 8, which depend also indirectly on the shifts of R_c.

Experiment	E-I	E-II	E-III	E-IV	E-V
$10^3\epsilon_a$	−0.18	−0.08	−0.01	−3.17	−11.12
$10^3\epsilon_r$	12.40	2.80	0.60	308.4	(2997)
$10^3\epsilon_{T'}$	17.1	3.94	0.82	424.3	(43594)
$10^3\epsilon_b$	43.2	10.44	2.06	(1047)	(7360)

TABLE 8. Fully numerical stability limits $\epsilon_a, \epsilon_r, \epsilon_{T'}, \epsilon_b$ for the experiments E-I, E-II, etc. The data in parentheses are of low accuracy (see § 4.1).

A detailed comparison between theory and the experiments was presented already in § 4. It shows that the Busse parameter Q continues to be a valuable measure for describing a strong NOB system in the weakly nonlinear regime, though the quantitative deviations are not small in some of the experimental runs. In any case the nonlinear properties have been captured only within an amplitude-equation approximation. Fully nonlinear analyses for the present system would be important to estimate the range of validity of weakly nonlinear analysis, by which only the amplitude instability of rolls and hexagons can be tested. In fact the importance of additional sideband instabilities has been emphasized in a recent fully nonlinear analysis in the case of weak NOB effects (Madruga *et al.* 2007; Madruga & Riecke 2007).

7. Conclusion

In this paper we discussed strong NOB effects that occur in RBC for instance of a fluid slightly above the critical point where the properties depend strongly and nonlinearly on the temperature. There the conventional OB approximation fails and the usual weakly nonlinear treatment of the NOB effects as given by Busse (1967) had to be replaced by a more sophisticated treatment.

The material properties of the fluid can be divided into two disjoint parts that differ with respect to the reflection symmetry about the midplane of the fluid layer. The odd part, if present, yields near-negligible shifts of the critical Rayleigh number R_c and wavenumber q_c and is responsible for the classical NOB scenario characterized by a transcritical bifurcation to hexagons near onset, with the hexagons replaced by rolls at larger R. The impact of the even part, on the other hand, to our knowledge had not been analysed in the literature. Although it preserves the supercritical bifurcation to rolls of the Boussinesq system, it leads to a significant shift of R_c.

For SF_6 the properties near the critical point are relatively well known. Thus this fluid was used for measurements, and in parallel its properties were used for specific calculations of the corresponding NOB effects. Very small changes of the average temperature T_m and the pressure P_{is} are sufficient to tune the system with respect to the even and odd NOB terms. The latter become very small if the average density ρ_m of the fluid is kept equal to the critical density ρ^*, leading to a bifurcations to rolls (as opposed to hexagons) near onset and to a sizable shift of ΔT_c.

In general the experimentally observed patterns and bifurcation points that we report in the present paper were convincingly confirmed by the theoretical analysis. We note that we did not observe the bifurcation sequence hexagons-rolls-hexagons ('re-entrant hexagons') with increasing ϵ that was described by Roy & Steinberg (2002) for experiments using SF_6. We find it doubtful that compressibility effects, which should not be relevant according to § 5.1, can be advocated (as they were by

Roy & Steinberg 2002) to explain this scenario. In contrast to the present work, where pressure and temperatures (and via the equation of state thus also the density) were externally controlled, it seems likely to us that one or more of these parameters were not strictly kept fixed by the experimental procedure used by Roy and Steinberg. In that case for instance the parameter a in (6.3), which measures the odd NOB effects, could effectively depend on ϵ and non-generic bifurcation sequences might become possible since the stability limits $\epsilon_a, \epsilon_b, \epsilon_r$ would depend, via a, on ϵ as well (see (A 1)). Note that alternatively the phenomenon of reentrant hexagons was predicted theoretically on the basis of a fully nonlinear analysis of Busse's classical NOB model (Madruga *et al.* 2007; Madruga & Riecke 2007). However, this theoretical work predicts wavenumbers smaller than the experimental ones (Roy & Steinberg 2002) for the reentrant hexagons at larger ϵ.

As a byproduct we also re-examined the classical weak NOB effects which had been studied most systematically by Busse (1967). Apart from a difference for one of the Busse coefficients we confirmed his results for infinite Prandtl number σ and in addition calculated the correction terms for finite σ.

The experimental work was supported by the US National Science Foundation through Grant DMR07-02111. One of the authors (W. Pesch) is very grateful to Professor Busse for many fruitful discussions about NOB convection. G. Ahlers acknowledges also the support of the Alexander von Humboldt Foundation, as well as the kind hospitality of the physical institute of the University of Bayreuth and the Max Planck Institute for Dynamics and Self-organization, Göttingen, where part of this work was performed.

Appendix A. Stability limits

The stability boundaries of hexagons and rolls are determined by the coefficients a, b, c of the amplitude equations (6.3) (see e.g. Busse 1967; Ciliberto *et al.* 1988; Malomed, Nepomnyashchy & Tribelsky 1990; Bodenschatz *et al.* 1991):

$$\epsilon_a = -\frac{a^2}{4(2b+c)}; \quad \epsilon_b = \frac{a^2(b+2c)}{(b-c)^2}; \quad \epsilon_r = \frac{a^2 c}{(b-c)^2}. \tag{A 1}$$

The equations for the amplitudes A_i are associated with a Lyapunov functional $\mathscr{F}$. Coexistence of the various states (rolls, hexagons, conduction state) imply equal values of the corresponding Lyapunov functionals. For $\epsilon = \epsilon_{T'}$ hexagons and the basic state coexist ($\mathscr{F}(0) = \mathscr{F}(A_h)$), while for $\epsilon = \epsilon_T$ hexagons and rolls coexist ($\mathscr{F}(A_r) = \mathscr{F}(A_h)$). The explicit expressions for $\epsilon_{T'}, \epsilon_T$ read as follows (see e.g. Malomed *et al.* 1990):

$$\epsilon_{T'} = \frac{8}{9}\epsilon_a, \tag{A 2}$$

$$\epsilon_T = \frac{a^2\left[\sqrt{c}(2(b+c))^{3/2} + 2c(3b+c)\right]}{4(2b+c)(b-c)^2}. \tag{A 3}$$

Note that ϵ_T given by (A 3) can be transformed into the expression given by Bodenschatz *et al.* (1991).

Appendix B. General formalism

In this appendix we present our method to calculate the amplitude equations. Up to minor technical modifications, we follow in great detail the calculational scheme used by Cross (1980).

Since the linear operators $\widehat{\mathscr{B}}, \widehat{\mathscr{L}}$ in the general NOB problem (5.21) are not self-adjoint we have to consider the adjoint eigenvalue problem as well. We use a standard hermitian scalar product, $\ll \cdot \mid \cdot \gg$ in position space, which simplifies for symbolic vectors $\hat{\boldsymbol{X}}(\boldsymbol{x}, z), \hat{\boldsymbol{Y}}(\boldsymbol{x}, z)$ of the form $\mathrm{e}^{\mathrm{i}\boldsymbol{q}_1\cdot\boldsymbol{x}}\boldsymbol{X}(z)$, $\mathrm{e}^{\mathrm{i}\boldsymbol{q}_2\cdot\boldsymbol{x}}\boldsymbol{Y}(z)$ as follows:

$$\ll \hat{\boldsymbol{X}} | \hat{\boldsymbol{Y}} \gg \equiv \delta_{\boldsymbol{q}_1,\boldsymbol{q}_2} \langle \boldsymbol{X} | \boldsymbol{Y} \rangle, \tag{B 1}$$

where $\delta_{\boldsymbol{q}_1,\boldsymbol{q}_2}$ denotes the Kronecker symbol.

The scalar product $\langle \boldsymbol{X} | \boldsymbol{Y} \rangle$ in Fourier space is defined as

$$\langle \boldsymbol{X} | \boldsymbol{Y} \rangle = \frac{2}{\pi} \int_{-1/2}^{1/2} \mathrm{d}z \boldsymbol{X}^{\dagger}(z) \boldsymbol{Y}(z). \tag{B 2}$$

Thus the adjoint operator $O^{\dagger}$ of an operator O is defined as follows:

$$\langle \boldsymbol{X} | O\boldsymbol{Y} \rangle = \langle O^{\dagger}\boldsymbol{X} | \boldsymbol{Y} \rangle, \tag{B 3}$$

where $\boldsymbol{X}, \boldsymbol{Y}$ correspond to the same wave vector $\boldsymbol{q}$.

Inspection of the linear problem (5.25) shows that the eigenvectors $\boldsymbol{U}_i^{\dagger}(\boldsymbol{q}, z)$ of the adjoint problem, which are determined by

$$\Lambda_i^*(\boldsymbol{q}, R)\mathscr{B}^{\dagger}\boldsymbol{U}_i^{\dagger}(\boldsymbol{q}, z) = \mathscr{L}^{\dagger}(\boldsymbol{q}, R)\boldsymbol{U}_i^{\dagger}(\boldsymbol{q}, z), \tag{B 4}$$

obey the boundary conditions (5.22) as well. Since in our case all eigenvalues Λ_i turn out to be real, the $\boldsymbol{U}_i^{\dagger}$ can be chosen to be real as well.

The following orthogonality conditions hold:

$$\langle \boldsymbol{U}_i^{\dagger} | \mathscr{B}\boldsymbol{U}_j \rangle = \langle \boldsymbol{U}_i^{\dagger} | \mathscr{L}\boldsymbol{U}_j \rangle = 0 \quad \text{if } i \neq j. \tag{B 5}$$

The normalization of the $\boldsymbol{U}_i^{\dagger}$ is fixed by $\langle \boldsymbol{U}_i^{\dagger} | \mathscr{B}\boldsymbol{U}_i \rangle = 1$. The correlation time τ_0 is defined as

$$\Lambda_0(\boldsymbol{q}_c, R) = < \boldsymbol{U}_0(\boldsymbol{q}_i, R) | \mathscr{L}\boldsymbol{U}_0(\boldsymbol{q}_i, R)) = \tau_0^{-1} \frac{(R - R_c)}{R_c} \tag{B 6}$$

for $\epsilon = (R - R_c)/R_c \approx 0$. Thus the expansion coefficients $A_i(t)$ of the solution $\hat{\boldsymbol{V}}$ of (5.21) are obtained as

$$A_i(t) = \langle \boldsymbol{U}_0(\boldsymbol{q}_i) | \mathscr{B}\mathrm{e}^{-\mathrm{i}\boldsymbol{q}_i x}\hat{\boldsymbol{V}} \rangle. \tag{B 7}$$

Up to the redefinition of the scalar product the further steps to expand (5.21) in terms of the $A_i(t)$ up to cubic order can be taken over from Cross (1980). One has, for instance, to calculate nonlinear solutions quadratic in the amplitudes A_i and $A_j(A_j^*)$ with the wave vectors $\boldsymbol{q}_i \pm \boldsymbol{q}_j$, $i, j = 1, 2, 3$ by inserting (6.1) into (5.21). Note, that these solutions have to be restricted to the subspace spanned by the eigenvectors $\boldsymbol{U}_i$ with $i \neq 0$ (see also Haken 1996; Plaut & Pesch 1999).

REFERENCES

Ahlers, G. 1980 Effect of departures from the Oberbeck–Boussinesq approximation on the heat transport of horizontal convecting fluid layers. *J. Fluid Mech.* **98**, 137–148.

Ahlers, G. 2006 Experiments with Rayleigh–Bénard convection. In *Dynamics of Spatio-Temporal Cellular Structures – Henri Bénard Centenary Review* (ed. I. Mutabazi, J. E. Wesfreid & E. Guyon), vol. 207, pp. 67–94. Springer.

Ahlers, G., Brown, E., Fontenele Araujo, F., Funfschilling, D., Grossmann, S. & Lohse, D. 2006 Non-Oberbeck–Boussinesq effects in strongly turbulent Rayleigh–Bénard convection. *J. Fluid Mech.* **569**, 409–445.

Ahlers, G., Calzavarini, E., Fontenele Araujo, F., Funfschilling, D., Grossmann, S., Lohse, D. & Sugiyama, K. 2008 Non-Oberbeck–Boussinesq effects in turbulent thermal convection in ethane close to the critical point. *Phys. Rev.* E **77**, 046302–1–16.

Ahlers, G., Fontenele Araujo, F., Funfschilling, D., Grossmann, S. & Lohse, D. 2007 Non-Oberbeck–Boussinesq effects in gaseous Rayleigh–Bénard convection. *Phys. Rev. Lett.* **98**, 054501–1–4.

Ahlers, G. & Oh, J. 2003 Critical phenomena near bifurcations in nonequilibrium systems. *Intl J. Mod. Phys.* B **17**, 3899–3908.

Ashkenazi, S. & Steinberg, V. 1999 High Rayleigh number turbulent convection in a gas near the gas–liquid critical point. *Phys. Rev. Lett.* **83**, 3641–3644.

Assenheimer, M. & Steinberg, V. 1993 Rayleigh–Bénard convection near the gas–liquid critical point. *Phys. Rev. Lett.* **70**, 3888–3891.

Bodenschatz, E., de Bruyn, J. R., Ahlers, G. & Cannell, D. S. 1991 Transition between patterns in thermal convection. *Phys. Rev. Lett.* **67**, 3078–3081.

Bodenschatz, E., Cannell, D. S., de Bruyn, J. R., Ecke, R., Hu, Y., Lerman, K. & Ahlers, G. 1992 Experiments on three systems with non-variational aspects. *Physica* D **61**, 77–93.

Bodenschatz, E., Pesch, W. & Ahlers, G. 2000 Recent developments in Rayleigh–Bénard convection. *Annu. Rev. Fluid Mech.* **32**, 709–778.

Boussinesq, J. 1903 *Theorie analytique de la chaleur, Vol. 2*. Gauthier-Villars.

de Bruyn, J. R., Bodenschatz, E., Morris, S. W., Trainoff, S., Hu, Y., Cannell, D. S. & Ahlers, G. 1996 Apparatus for the study of Rayleigh–Bénard convection in gases under pressure. *Rev. Sci. Instrum.* **67**, 2043–2067.

Busse, F. H. 1967 The stability of finite amplitude cellular convection and its relation to an extremum principle. *J. Fluid Mech.* **30**, 625–649.

Ciliberto, S., Coullet, P., Lega, J. & Pampaloni, E. 1990 Defects in roll-hexagon competition. *Phys. Rev. Lett.* **65**, 2370–2373.

Ciliberto, S., Pampaloni, E. & Perez-Garcia, C. 1988 Competition between different symmetries in convective patterns. *Phys. Rev. Lett.* **61**, 1198–1201.

Cross, M. C. 1980 Derivation of the amplitude equation at the Rayleigh–Bénard instability. *Phys. Fluids* **23**, 1727–1730.

Gough, D. O. 1969 The anelastic approximation in thermal convection. *J. Atmos. Sci.* **26**, 448–456.

Haken, H. 1996 Slaving principle revisited. *Physica* D **97**, 95–103.

Hoard, C. Q., Robertson, C. R. & Acrivos, A. 1970 Experiments on the cellular structure in Bénard convection. *Intl J. Heat Mass Transfer* **13**, 849–856.

Hohenberg, P. C. & Swift, J. S. 1992 Effects of additive noise at the onset of Rayleigh–Bénard convection. *Phys. Rev.* A **46**, 4773–4785.

Hoogland, J. H. B., van den Berg, H. R. & Trappeniers, N. J. 1985 Measurements of the viscosity of sulfur hexaflouride up to 100 bar by a capillary-flow viscometer. *Physica* A **134**, 169–192.

Kestin, J. & Imaishi, N. 1985 Thermal conductivtity of sulfurhexafluoride. *Intl J. Thermophys.* **6**, 107–118.

Kogan, A. B. & Meyer, H. 2001 Heat transfer and convection onset in a compressible fluid: ^{3}He near the critical point. *Phys. Rev.* E **63** (056310), 1–15.

Landau, L. D. & Lifshitz, E. M. 1987 *Fluid Mechanics*. Pergamon.

Lim, T. K., Swinney, H. L., Langley, K. H. & Kachnowski, T. A. 1971 Rayleigh linewidth in SF_6 near the critical point. *Phys. Rev. Lett.* **27**, 1776–1779.

Lis, J. & Kellard, P. O. 1965 Measurements of the thermal conductivity of sulphur hexafluoride and 50 % (volume) mixture of sulphur hexafluoride and nitrogen. *Br. J. Appl. Phys.* **16**, 1099–1104.

Madruga, S. & Riecke, H. 2007 Hexagons and spiral-defect chaos in non-Boussinesq convection at low Prandtl numbers. *Phys. Rev.* E **75**, 026210–1–14.

Madruga, S., Riecke, H. & Pesch, W. 2007 Reentrant hexagons in non-Boussinesq convection. *J. Fluid. Mech* **548**, 341–360.

Malomed, B. A., Nepomnyashchy, A. A. & Tribelsky, M. I. 1990 Domain boundaries in convection patterns. *Phys. Rev.* A **42**, 7244–7263.

Oberbeck, A. 1879 Über die Wärmeleitung der Flüssigkeiten bei Berücksichtigung der Strömungen infolge von Temperaturdifferenzen. *Ann. Phys. Chem.* **7**, 271–292.

Oh, J. & Ahlers, G. 2003 Thermal-noise effect on the transition to Rayleigh-Bénard convection. *Phys. Rev. Lett.* **91** (094501), 1–4.

Oh, J., Ortiz de Zárate, J. M., Sengers, J. V. & Ahlers, G. 2004 Dynamics of fluctuations in a fluid below the onset of Rayleigh–Bénard convection. *Phys. Rev.* E **69**, 021106.

Pampaloni, E., Perez-Garcia, C., Albavetti, L. & Ciliberto, S. 1992 Transition from hexagons to rolls in convection in fluids under non-Boussinesq conditions. *J. Fluid Mech.* **234**, 393–416.

Perez-Garcia, C., Pampaloni, E. & Ciliberto, S. 1990 Finite-size effects in the transition from hexagons to rolls in convective systems. *Europhys. Lett.* **12**, 51–55.

Plaut, E. & Pesch, W. 1999 Extended weakly nonlinear theory of planar nematic convection. *Phys. Rev.* E **59**, 1747–1469.

Roy, R. & Steinberg, V. 2002 Reentrant hexagons in non-Boussinesq Rayleigh–Bénard convection: effect of compressibility. *Phys. Rev. Lett.* **88**, 244903–1–4.

Schlüter, A., Lortz, D. & Busse, F. H. 1965 On the stability of steady finite amplitude convection. *J. Fluid Mech.* **23**, 129–144.

Strehlow, T. & Vogel, E. 1989 Temperature dependence and initial density dependence of the viscosity of sulphur hexafluoride. *Physica* A **161**, 101–117.

Sugiyama, K., Calzavarini, E., Grossmann, S. & Lohse, D. 2007 Non-Oberbeck–Boussinesq effects in two-dimensional Rayleigh–Bénard convection in glycerol. *Europhys. Lett.* **80** (34002), 1–6.

Swift, J. & Hohenberg, P. C. 1977 Hydrodynamic fluctuations at the convective instability. *Phys. Rev.* A **15**, 319–328.

Swinney, H. L. & Henry, D. L. 1973 Dynamics of fluids near the critical point: decay rate of order-parameter fluctuations. *Phys. Rev.* A **8**, 2586–2617.

Trainoff, S. P. & Cannell, D. S. 2002 Physical optics treatment of the shadowgraph. *Phys. Fluids* **14**, 1340–1363.

Tschammer, A. 1996 Nichtlineare Aspekte der Rayleigh–Bénard Konvektion in isotropen und anisotropen Fluiden. PhD thesis, Universität Bayreuth, Bavaria.

Walden, R. W. & Ahlers, G. 1981 Non-Boussinesq and penetrative convection in a cylindrical cell. *J. Fluid Mech.* **109**, 89–114.

Wu, X. Z. & Libchaber, A. 1991 Non-Boussinesq effects in free thermal convection. *Phys. Rev.* A **43**, 2833–2839.

Wyczalkowska, A. K. & Sengers, J. V. 1999 Thermodynamic properties of sulfur hexafluoride in the critical region. *J. Chem. Phys.* **111**, 1551–1560.

Zhang, J., Childress, S. & Libchaber, A. 1997 Non-Boussinesq effect: thermal convection with broken symmetry. *Phys. Fluids* **9**, 1034–1042.

Zhang, J., Childress, S. & Libchaber, A. 1999 Non-Boussinesq effect: asymmetric velocity profiles in thermal convection. *Phys. Fluids* **10**, 1534–1536.